Cholinergic Modulation of Chandelier Cells via Heteromeric Nicotinic Receptors in Prefrontal Cortex

Emilio Martinez-Marquez, Santiago Reyes-Leon, Flores Garcia-San-Jose, Santiago Lopez-Begines, Jose L Nieto-Gonzalez, Pablo Garcia-Junco-Clemente.

Instituto de Biomedicina de Sevilla (IBiS, Hospital Universitario Virgen del Rocío/CSIC/Universidad de Sevilla), Dpto. de Fisiología Médica y Biofísica, Facultad de Medicina, and CIBERNED ISCIII, Seville, Spain

Correspondence to:

jlnieto@us.es

pablo_gjc@us.es

Abstract

Chandelier cells (ChCs) are a distinct subtype of GABAergic interneurons that form vertical arrays of presynaptic boutons targeting the axon initial segment (AIS) of pyramidal neurons (PNs). They are particularly abundant in prefrontal cortex, where cholinergic inputs modulate cognitive functions and shape ChC axonal development. However, the effects of the cholinergic system on ChC activity in the adult brain remain largely unexplored. Here, using a genetic intersectional strategy (*VipR2-Pvalb-Ai65*) in adult mice, we selectively labeled ChCs in the secondary motor cortex (M2). Immunohistochemistry and electrophysiology confirmed morphological and functional properties distinguishing them from basket cells. We found that these ChCs exhibit an inward current in response to nicotinic acetylcholine receptor (nAChR) agonists. Pharmacological blockade and fluorescent in situ hybridization revealed that this effect is primarily mediated by heteromeric nAChRs containing β2 subunits, with a smaller contribution from α3 subunits. Optogenetic stimulation of basal forebrain (BF) cholinergic axons evoked inward currents in ChCs, confirming a functional cholinergic drive. Furthermore, in vivo two-photon calcium imaging revealed a strong correlation between ChC activity and behavioral markers of arousal, including locomotion and pupil dilation. Importantly, the application of nicotinic receptor antagonists significantly diminished ChC activity during movement. Together, these results indicate that ChCs are modulated by cholinergic input via heteromeric nAChRs, emphasizing their importance in facilitating state-dependent cortical dynamics.

Introduction

The mammalian cerebral cortex is a highly complex structure consisting of excitatory and inhibitory neurons that form intricate networks essential for brain function. Excitatory PNs, which constitute approximately 85–90% of all cortical neurons, are primarily responsible for transmitting information between cortical areas and relaying signals from the cortex to other brain regions (Marín, 2012; Tremblay et al., 2016). In contrast, inhibitory GABAergic interneurons, although comprising only 10-20% of cortical neurons, play a crucial role from controlling hyperexcitability to fine-tuning synaptic integration, spike timing and temporal coordination within cortical circuits (Cardin, 2018; Isaacson and Scanziani, 2011; Meyer et al., 2011; Roux and Buzsáki, 2015; Rudy et al., 2010). These interneurons are traditionally classified based on morphological and electrophysiological properties, with key molecular markers such as parvalbumin, somatostatin, and the ionotropic serotonin receptor 5HT3a defining major subtypes (Josh Huang and Paul, 2019; Rudy et al., 2010; Tremblay et al., 2016). Despite advances in interneuron classification, significant heterogeneity exists within these groups, leaving the precise contributions of many interneuron subtypes unresolved.

Among GABAergic interneurons, ChCs, also known as axo-axonic interneurons, are particularly notable due to their highly specialized connectivity (Somogyi, 1977). ChCs are a subclass of parvalbumin-expressing interneurons, although it has been reported that some ChCs may exhibit weak or negligible parvalbumin expression (Taniguchi et al., 2013), underscoring the complexity of interneuron classification. These interneurons specifically target the AIS of PNs, a critical site for action potential

initiation, allowing ChCs to exert significant influence on neuronal output and network activity (Howard et al., 2005; Kole and Stuart, 2012; Lu et al., 2017; Veres et al., 2014). The functional role of ChCs in the cortical network remains largely unknown due to the lack of specific markers to identify and modulate these interneurons, preventing a systematic analysis. However, recent genetic strategies have improved the targeting of this cell type, allowing the introduction of genetically encoded tools to manipulate the ChCs. Key tools available to study ChCs include the Nkx2.1-CreER (Lu et al., 2017; Taniguchi et al., 2013; Wang et al., 2019), the Vipr2-Cre (Daigle et al., 2018; Nakashima et al., 2022; Schneider-Mizell et al., 2021; Seignette et al., 2024), the Unc5b-CreER (Dudok et al., 2021) and a novel intersectional genetic strategy for targeting AACs based on lineage and molecular markers (Raudales et al., 2024). These tools have helped to demonstrate that ChCs integrate inputs from both local excitatory and inhibitory neurons as well as higher-order cortical regions, emphasizing their role as integrative hubs in cortical networks (Jung et al., 2022; Lu et al., 2017).

Acetylcholine (ACh) is a key neuromodulator in the central nervous system, critically involved in regulating arousal, attention, and learning by modulating neuronal excitability, synaptic integration, and circuit plasticity (Ballinger et al., 2016; Colangelo et al., 2019; Hangya et al., 2015; Hasselmo and Sarter, 2011; Lee and Dan, 2012). The BF serves as the principal source of cholinergic input to the cortex, with projections primarily targeting superficial layers, including layer 1 (Ananth et al., 2023; Ballinger et al., 2016; Gielow and Zaborszky, 2017). Notably, ChCs reside at the layer (L)1–L2/3 boundary, extending their dendritic branches within the lamina and sending a prominent dendrite upward into L1 (Taniguchi et al., 2013; Woodruff et al., 2011). Indeed, prefrontal L1 contains one of the highest laminar densities of cholinergic axons and varicosities (Mechawar et al., 2000), suggesting that ChCs may be strongly

influenced by the cholinergic system, which is critically involved in the regulation of brain network states. Supporting this notion, ChCs have been shown to receive direct synaptic input from the diagonal band (Lu et al., 2017). Elevated cholinergic tone characterizes high-arousal states, often reflected in behavioral readouts such as locomotion or pupil dilation (Fu et al., 2014; McGinley et al., 2015a; Reimer et al., 2016; Vinck et al., 2015). Specifically, ChCs exhibit heightened activity during high-arousal conditions, such as locomotion, across cortical regions including the hippocampus, visual cortex, and M2 (Dudok et al., 2021; Jung et al., 2023; Schneider-Mizell et al., 2021; Seignette et al., 2024). Moreover, cholinergic signaling governs the axonal arborization of ChCs during development (Steinecke et al., 2022). Taken together, these findings highlight the possible role of cholinergic modulation in orchestrating ChC activity and position ChCs at the intersection of local circuit dynamics and global neuromodulatory influences during behaviorally relevant, high-arousal states.

In this study, we analyzed ChCs in L2/3 of M2 to systematically investigate whether and how they are directly modulated by the cholinergic system. We selectively labeled ChCs, using an intersectional genetic approach (Vipr2-Pvalb-Ai65), for comprehensive morphological, electrophysiological, and immunohistochemical characterization. We then combined *in vitro* recordings, *in vivo* imaging, and optogenetic manipulations to ascertain the mechanisms of ChC modulation via nAChRs. Our findings reveal that M2 ChCs express functional heteromeric nAChRs, exhibit robust depolarization under cholinergic drive, and display activity patterns tightly associated with key indicators of arousal, such as locomotion and pupil dilation. By elucidating how neuromodulatory signals directly regulate ChC excitability at the

AIS of PNs, this work provides new insights into the specialized role of ChCs in shaping cortical output during behaviorally relevant, high-arousal states.

Results

Assessment of the VipR2-Pvalb-Ai65 Mouse Model for Precise Targeting of Chandelier Cells

Before exploring the role of cholinergic modulation in ChCs, we employed a genetic targeting approach to enable their visualization and detailed characterization. This approach applied a genetic intersection method combining the vasoactive intestinal peptide receptor 2 (*Vipr2)* and parvalbumin (*Pvalb*) promoters, as previously described by Tasic et al. (2018). Specifically, CRE recombinase was driven by the *Vipr2* promoter, which is selectively expressed in adult ChCs (Daigle et al., 2018; Schneider-Mizell et al., 2021), while FLP recombinase (FlpO) was driven by the *Pvalb* promoter, a well-established marker for parvalbumin expressing interneurons, including ChCs (Inan and Anderson, 2014). To visualize the ChCs, we crossed the *Vipr2-Pvalb* mice with the Ai65 reporter line ($VipR2^{Cre\ +/-}$-$Pvalb^{flp\ +/-}$-$Ai65^{+/-}$), resulting in mice that expressed the tdTomato fluorescent reporter (tdTomato^{+}) in cells co-expressing both Cre and FLP recombinases (Tasic et al., 2018). Subsequent immunostaining and electrophysiological analysis were performed to verify that the labeled neurons corresponded to ChCs.

The somatic tdTomato labeling was predominantly observed at the boundary of cortical layers L1 and L2/3 (Figure 1A), a region densely populated by ChCs (Inan and Anderson, 2014). Notably, tdTomato^{+} cells displayed the hallmark features of ChCs (figure 1B, left panel). Using the Filament Tracer tool in Imaris software, we reconstructed their dendritic and axonal architecture (figure 1B, right panel). The

axonal arborization revealed the formation of vertical arrays of presynaptic terminals, known as cartridges, while the dendrites extended vertically into L1. These structural characteristics align with previously documented descriptions of ChCs (Taniguchi et al., 2013; Woodruff et al., 2011). To evaluate the ability of ChCs to target the AIS of PNs, we conducted immunofluorescence staining for the phosphorylated form of IκBα (p-IkBα), a marker enriched in the AIS (Schultz et al., 2006; Taniguchi et al., 2013). Surface-surface contact analysis using Imaris algorithms revealed interactions between tdTomato and p-IkBα (a surface contact area of 1672,45 ± 595,03 μm^2, representing a 13,86 ± 4,81 % out of a total AIS surface area of 9563,64 ± 2127,15 μm^2), confirming that the axonal cartridges of ChCs establish synapses on the AIS of PNs—a distinctive feature of these interneurons. (figure 1C-E)

Given that ChCs are traditionally classified within the parvalbumin interneuron group, we performed immunofluorescence experiments to assess the degree of colocalization between parvalbumin-expressing neurons and tdTomato-labeled cells (figure 1F-I). Quantification revealed that 90% of parvalbumin positive cells (4 mice, 32 slices) were negative for tdTomato (figure 1I), indicating that ChCs represent a minority subgroup within parvalbumin neurons. Additionally, 80% of tdTomato$^+$ cells (4 mice, 32 slices) were parvalbumin positive, supporting their expected ChC identity. Interestingly, 20% of tdTomato$^+$ cells did not colocalize with parvalbumin$^+$ neurons (figure 1I), suggesting variability in parvalbumin expression among ChCs in the neocortex, consistent with previous findings (Taniguchi et al., 2013). It would indicate that, using our targeting strategy, we may be selecting a subset of ChCs (*VipR2*$^+$-*Pvalb*$^+$).

To functionally characterize the putative ChCs, we conducted electrophysiological recordings of tdTomato$^+$ cells located at the boundaries of cortical layers L1 and L2/3.

Fluorescence-guided whole-cell patch-clamp recordings were employed to confirm the neuronal identity (figure 1J). Passive and active membrane properties were measured using current-clamp recordings (figure 1K). On average, tdTomato$^+$ cells exhibited characteristics consistent with those reported for fast-spiking ChCs (Taniguchi et al., 2013; Woodruff et al., 2009; Xu and Callaway, 2009), including their firing patterns and intrinsic properties. These included a resting membrane potential of -71.52 ± 0.48 mV (n = 32), input resistance of 129.95 ± 5.96 MΩ (n = 32), time constant of 6.51 ± 0.24 ms (n = 32), rheobase of 206.50 ± 13.09 pA (n = 32), afterhyperpolarization (AHP) amplitude of 23.22 ± 0.45 mV (n = 32) (Figure 1—figure supplement 1).

Basket cells (BCs) are the predominant group of fast-spiking parvalbumin interneurons (Rudy et al., 2010). To further validate our mouse model and exclude the potential labeling of BCs, we compared the electrophysiological properties of our putative ChCs with those of BCs. For this, we utilized the *PVCre-Ai14* mouse model, which expresses tdTomato in both groups of parvalbumin positive interneurons. Recordings were conducted on putative BCs in layer 2/3 of M2, avoiding the L1/L2/3 boundary region (Figure 1—figure supplement 1). BCs displayed a stronger fast-spiking phenotype compared to the putative ChCs, and they exhibited distinct electrophysiological parameters. These results suggest that the *VipR2-Pvalb-Ai65D* mouse model is a reliable tool for detailed anatomical and functional analyses of ChCs.

Direct Modulation of Chandelier Cells by Nicotinic Acetylcholine Receptors.

ChCs possess dendrites that extend into L1, suggesting they act as circuit switches by integrating inputs from cortical areas. The dense cholinergic innervation in L1 suggests that ChCs could be influenced by cholinergic modulation.

To explore this, we conducted whole-cell patch-clamp recordings in M2 brain slices, targeting ChCs labeled with tdTomato. Using a current-clamp configuration, bath

application of the cholinergic agonist carbachol (25 μM) (Figure 2—figure supplement 1A) induced a reversible depolarization of the ChCs resting membrane potential (8,24 ± 0,22 mV, n = 10). Similar results were observed with the nicotinic agonist DMPP (25 μM), suggesting the involvement of nAChRs (Figure 2—figure supplement 1B) (10,18 ± 0,27 mV, n = 17). Remarkably, the depolarizing response to DMPP persisted despite the application of a blocking solution containing TTX (1 μM), CNQX (10 μM), DL-APV (50 μM), picrotoxin (50 μM), and atropine (4 μM), confirming that the effect was independent of synaptic transmission and specific for nicotinic modulation (Figure 2—figure supplement 1C) (6,87 ± 0,60 mV, n = 20). To confirm that the depolarization of ChCs was primarily mediated by the activation of nAChRs, we performed voltage-clamp recordings while applying DMPP via local pressure (100 μM, 20 ms, 4 psi; figure 2A). This application elicited an inward current in normal ACSF (figure 2B; amplitude: -76.38 ± 7,89 pA, n = 23) that persisted in the presence of the previously described blocking solution (figure 2B; amplitude: -47,37 ± 4,69 pA, n = 23). Notably, the inward current was abolished upon the addition of mecamylamine (MMA, 5 μM), a specific nAChR antagonist (figure 2B; amplitude: N/A, n = 23). These findings confirm the key role of nAChRs in mediating the observed response.

Heteromeric Nicotinic Receptors Mediate the Cholinergic Response in Chandelier Cells

Previous studies, including transcriptomic analyses, have reported the presence of cholinergic receptor subunits in ChCs (Krenz et al., 2001; Rybnicek et al., 2024; Tasic et al., 2018). However, the exact composition of these receptor subunits remains elusive.

In the cortex, nACHRs are classified as either homopentameric α7 receptors or heteromeric α4β2 receptors (Albuquerque et al., 2009; Cecilia Gotti, 2006), which may

also incorporate α5 subunits. To investigate the presence of nAChRs on ChCs, we performed fluorescent in situ hybridization (FISH: figure 2C-D). To enhance the number of ChCs available for this quantification, we modified our experimental approach slightly. Using the same mouse model (*VipR2Cre*$^{+/-}$-*Pvalbflp*$^{+/-}$-*Ai65*$^{+/-}$), we stereotaxically injected a floxed-tdTomato AAV (AAV9-hSynP-Flex-TdTomato) into the M2 region. Three weeks after the injection, the FISH experiments were performed. The majority of ChCs (73.78%, n = 166/229) expressed the β2 nicotinic receptor subunit (CHRNB2), with a mean fluorescence intensity of 29,82 ± 0,9 a.u. (figure 2C). A smaller subset of ChCs expressed the α7 subunit (CHRNA7, 17.86%, n = 20/112), also with a mean fluorescence intensity of 15,88 ± 1,55 a.u. These findings suggest that heteromeric nAChRs are the predominant subtype in ChCs. To further dissect the contributions of specific nAChR subunits, we performed patch-clamp recordings using the protocol described in figure 2A but applying subunit-specific blockers instead of a general nAChR antagonist (figure 2F-I). To assess the role of the β2 subunit, DMPP application under control conditions evoked an inward current with a peak amplitude of –125.83 ± 25.99 pA (n = 10). This response was reduced to –78.96 ± 13.94 pA ($p < 0.01$ compared to control, n = 10) following the blockage of synaptic transmission and further attenuated to –42.04 ± 6.91 pA ($p < 0.01$, n = 10) upon the addition of DHβE (10 μM), a selective antagonist of β2-containing nAChRs, to the ACSF (figure 2F).

To investigate the role of the α7 subunit, we applied DMPP under control conditions, which elicited an inward current with an amplitude of –64,97 ± 6,86 pA (n = 10). This response was reduced after blocking synaptic transmission (–49,38 ± 6,21 pA, $p<0.01$, n = 10) but remained unaffected by the addition of methyllycaconitine (MLA), a selective antagonist of α7-containing nAChRs (200 nM, –48,39 ± 6,18 pA, $p > 0.05$, n

= 10; Figure 2G). Given that α7-containing nAChRs are characterized by their rapid inward current kinetics (Arroyo et al., 2012), potentially overshadowed by the dominant β2-containing nAChRs, we further examined the inward current by sequentially applying DHβE and MLA. Under control conditions, the amplitude was –112.09 ± 11.29 pA (n = 6), which decreased to –62.19 ± 8.11 pA (n = 6) after blocking synaptic transmission in the presence of DHβE and to –56.61 ± 7.04 pA (n = 6) following the addition of MLA. The lack of a significant difference between the DHβE and DHβE + MLA conditions ($p > 0.05$; Figure 2H) indicates that α7-containing nAChRs have a limited role in the cholinergic modulation of ChCs. This result underscores the predominant involvement of β2-containing nAChRs in mediating the cholinergic regulation of ChCs.

Since a residual inward current persisted after blocking with MLA and DHβE, we hypothesized that additional heteromeric receptor subtypes might contribute to the nicotinic modulation of ChCs. Transcriptomic studies in the mouse cortex have previously reported the expression of the α3 subunit (CHRNA3) (Bugeon et al., 2022; Tasic et al., 2018). To investigate the potential involvement of α3 in heteromeric nAChRs, we performed fluorescent in situ hybridization, which confirmed the presence of α3 subunit in nearly 30% of ChCs (CHRNA3, 29.52%, n = 31 out of 105) with a mean fluorescence intensity of 36,57 ± 3,25 a.u (figure 2E). To assess the contribution of α3 subunits to the inward current, we applied tropinone, a specific α3 subunit blocker. Under control conditions, the inward current amplitude was –122,24 ± 28,32 pA (n = 10). This amplitude was reduced to –65,74 ± 15,32 pA ($p < 0.001$ compared to control, n = 10) after blocking synaptic transmission in the presence of DHβE and further decreased to –42,90 ± 10,62 pA ($p < 0.001$, n = 10) when tropinone (300 μM) was added alongside DHβE (figure 2I).

Collectively, these findings highlight the involvement of heteromeric nAChRs, including those containing the α3 subunit, in the cholinergic modulation of ChCs.

Optogenetic Stimulation of Basal Forebrain Cholinergic Axons Elicits an Inward Current in Chandelier Cells

The primary cholinergic nuclei projecting to the neocortex reside in the BF. To investigate whether these neurons form monosynaptic connections with M2 cortical ChCs and drive their nicotinic modulation, we applied optogenetic stimulation combined with electrophysiological recordings in brain slices.

We employed a transgenic mouse line that allows for the identification of cortical ChCs while simultaneously expressing CRE recombinase in cholinergic neurons (*VipR2*$^{Cre\ +/-}$-*Pvalb*$^{flp\ +/-}$-*Ai65*$^{+/-}$-*ChAT*$^{Cre+/-}$). To target cholinergic neurons, we injected AAVs carrying a floxed version of the optogenetic activator ChR2-YFP into the primary cholinergic nuclei (figure 3A–C). Three weeks post-injection, immunofluorescence analysis confirmed the presence of cholinergic axons expressing ChR2 in the M2 cortical region (figure 3D). Next, we conducted patch-clamp recordings of ChCs in brain slices while selectively photostimulating cholinergic axons projecting to the M2 region (figure 3D, insert). In voltage-clamp configuration, a 5-second photostimulation protocol elicited an inward current in ChCs under both ACSF and the previously described blocking solution. This response was completely abolished upon the addition of nicotinic antagonists (MMA, 5 μM; MLA, 200 nM; DHβE, 10 μM) to the blocking solution (figure 3E-F) (Mean amplitude under control conditions: -26,76 ± 6,19 pA. Mean amplitude after blocking solution: -19,21 ± 2,26 pA. Mean amplitude after nicotinic antagonists: N/A). These findings confirm that cholinergic axons originating from the BF modulate ChC activity.

Chandelier Cell Activity Correlates with High Arousal States in the M2 Cortex

Fluctuations in arousal states profoundly impact cortical activity and behavioral performance. ACh plays a pivotal role in these dynamics, modulating the activity of individual cortical neurons and orchestrating their interactions within neural networks. Cholinergic signaling is strongly linked to high-arousal states, which often accompany active behaviors such as locomotion, an observable measure of internal arousal levels, and spontaneous pupil diameter fluctuations that reflect shifts in vigilance, attention, and cognitive effort (McGinley et al., 2015b; Neyhart et al., 2024; Reimer et al., 2016, 2014).

To explore the relationship between ChCs activity and behavioral states, we utilized two-photon calcium imaging to monitor ChCs activity in awake, head-fixed mice navigating on a floating spherical treadmill (figure 4A). Behavioral metrics, including pupil diameter and running speed, were simultaneously recorded during imaging. To achieve this, we injected an adeno-associated viral vector encoding a CRE-dependent calcium indicator gene, GCaMP6s, into the M2 cortical region of adult *VipR2*$^{Cre\ +/-}$-*Pvalb*$^{flp\ +/-}$-*Ai65*$^{+/-}$ mice (figure 4A). Since CRE recombinase is expressed in these mice under the control of the *Vipr2* promoter, we observed GCaMP6s expression in both tdTomato^{+} (30,5%) and tdTomato^{-} (69,5%) cells. To determine whether tdTomato^{-} cells displayed ChC characteristics, we performed immunofluorescence against GCaMP6s, identifying the typical ChC morphology (figure 4B), consistent with previous studies (Schneider-Mizell et al., 2021). Additionally, 72.1% of GCaMP6s-positive cells were also positive for parvalbumin, while 27.9% were negative, further suggesting variability in parvalbumin expression among ChCs (3 mice and 15 slices; figure 4C).

Qualitative analysis of calcium signals from both tdTomato$^+$ and tdTomato$^-$ ChCs revealed increased activity during periods of treadmill running (figure 4D). To quantify the association between arousal state and ChC responses, we calculated correlation coefficients between the activity of both tdTomato$^+$ and tdTomato$^-$ ChCs and two key behavioral metrics: pupil size and running speed. Our analysis showed that all imaged neurons (tdTomato$^+$ and tdTomato$^-$) exhibited positive correlations with both pupil diameter and running speed (figure 4E and video 1). Since the degree of correlation did not significantly differ between the two populations, we combined them for subsequent analyses.

The correlation analysis between ChCs activity and individual behavioral metrics, such as running and pupil diameter, revealed a significantly stronger relationship with pupil size than with locomotion (figure 4F-G). This finding likely reflects that, during quiet periods, behavioral changes are not detected as overt movement but are instead linked to spontaneous fluctuations in pupil diameter (figure 4H). These fluctuations closely align with ChC activity, offering a more sensitive indicator of underlying neural dynamics. Previous studies have shown that pupil dynamics predict changes in oscillatory network activity and are reliably correlated with subthreshold membrane potential fluctuations in certain cortical neuron subtypes, even in the absence of overt movement (McGinley et al., 2015a). These Vm changes result from alterations in cholinergic and adrenergic inputs (Polack et al., 2013). Interestingly, pupil dynamics emerge as a robust proxy for tracking neuromodulatory changes within the cortex (Reimer et al., 2016). Given that we have demonstrated ChCs are modulated by cholinergic input, it is plausible to hypothesize that this neuromodulation has an important role for the proper functioning of the ChC population.

Cholinergic Blockade Attenuates Chandelier Cells Neuronal Responses to Locomotion

Cholinergic modulation plays a key role in shaping the activity of cortical interneurons neurons during behaviorally relevant states such as locomotion (Fu et al., 2014; Polack et al., 2013). Because ChCs are modulated by nAChRs, we checked how the blockade of cholinergic signaling impacts ChC responses during locomotion.

We performed in vivo two-photon calcium imaging of the same ChCs in the presence and absence of nicotinic antagonists (MMA, 1 mM; MLA, 0.1 mM) (Fu et al., 2014). Blocking nicotinic receptors led to a marked reduction in ChC responses during locomotion (Figure 5A). Cross-correlation analysis between calcium signals and treadmill movement showed a sharp decline after antagonist treatment (Zero-time cross-correlation: Control: 0.33 ± 0.03; MMA/MLA: 0.08 ± 0.03, $p<0.001$, $n = 20$) (figure 5B). Additionally, quantitative analysis revealed a significant decrease in the normalized amplitudes of calcium signals associated with movement following antagonist treatment (Control: 1.41 ± 0.17 SEM; MMA/MLA: 0.05 ± 0.13 SEM, $p<0.001$, $n = 20$) (figure 5C). These findings highlight the critical role of cholinergic inputs in modulating ChC activity and ensuring their proper tuning during active behavioral states.

Discussion

Our findings reveal that ChCs in the M2 cortical region are strongly modulated by cholinergic signaling through nAChRs, with this modulation closely tied to arousal states. This study advances our understanding of ChC function by highlighting the selective role of heteromeric nAChRs—particularly those containing β2 subunits and, to a lesser extent, α3 subunits—in regulating ChC excitability. Furthermore, our in vivo data demonstrates that ChC activity aligns with behavioral markers of arousal, such

as locomotion and pupil dilation. The marked reduction in ChC responses following nicotinic receptor blockade underscores the critical role of cholinergic inputs in fine-tuning ChC activity during active behavioral states. These findings suggest that cholinergic inputs are essential for integrating ChCs into cortical circuits, enabling neural dynamics that are finely tuned to behavioral states.

ChCs are among the least studied cortical GABAergic interneurons, a gap primarily due to their rarity and the historical lack of reliable genetic labeling tools (Dudok et al., 2021; Raudales et al., 2024; Taniguchi et al., 2013; Tasic et al., 2018). Several *in vivo* labeling strategies—ranging from single-transgenic to intersectional approaches—have been employed to target ChCs, each with its own advantages and limitations (Raudales et al., 2024). In this study, we used a genetic intersectional strategy to selectively target and visualize a subpopulation of parvalbumin-expressing ChCs in adult mice by combining *VipR2*- and *Pvalb*-driven recombinases with the *Ai65D* fluorescent reporter line (Tasic et al., 2018). Our immunohistochemical analyses indicate that approximately 80% of tdTomato$^+$ cells co-express parvalbumin, supporting their expected ChC identity. Notably, the remaining 20% of tdTomato$^+$ cells did not exhibit strong parvalbumin signals, underscoring variability in parvalbumin expression among ChCs in the neocortex—an observation consistent with previous reports (Taniguchi et al., 2013). These results suggest that, while our strategy effectively labels a substantial fraction of ChCs, it likely targets a specific subset of *Vipr2-Pvalb* ChCs and potentially underestimates the overall ChC population. This heterogeneity emphasizes the complexity of interneuron classification in the cortex and highlights the need for precise genetic tools for dissecting the diverse cellular phenotypes and functions of cortical inhibitory interneurons. The parvalbumin-positive interneuron subgroup is composed of both ChCs and BCs (Rudy et al., 2010;

Tremblay et al., 2016). By comparing *Vipr2*–*Pvalb*-labeled ChCs with BCs in a *Pvalb-Cre* model, we discerned electrophysiological signatures in ChCs, corroborating their specialized status within the parvalbumin interneuron subgroup (Povysheva et al., 2013; Taniguchi et al., 2013).

While the potential expression of nicotinic acetylcholine receptors in cortical basket cells remains unresolved, with conflicting evidence in the literature(Bloem et al., 2014; Poorthuis et al., 2013; Porter et al., 1999), our findings demonstrate that Chandelier cells (ChCs) undergo significant cholinergic modulation. One of the most striking observations is that direct activation of nAChRs, either pharmacologically (via carbachol or DMPP) or optogenetically (via BF cholinergic axon stimulation), evokes an inward current in ChCs. Importantly, these responses persist under synaptic blockers and are abolished by mecamylamine, a selective nAChR antagonist, demonstrating a direct postsynaptic action of ACh on ChCs. The primary nicotinic receptors in the cortex are homopentameric α7 and heteromeric α4β2 receptors. Our data show that α7-containing nAChRs play a minimal role in the cholinergic modulation of Chandelier cells (ChCs), as only a small fraction of ChCs express the α7 subunit, and MLA blockade does not significantly affect the inward current observed in electrophysiological recordings. In contrast, we detect robust β2 subunit expression in most ChCs, with a marked reduction in inward currents following blockade with DHβE. Interestingly, our results suggest the presence of α3-containing heteromeric nAChRs, likely α3β4, in cortical ChCs. While this receptor has been well-characterized in other brain regions(Cecilia Gotti, 2006), it has been less frequently reported in the cortex, although recent transcriptomic studies provide evidence for the presence of α3 in the mouse cortex(Bugeon et al., 2022; Tasic et al., 2018). Despite the small fraction of cells expressing α7 or α3, the prominent α3 signal in FISH experiments and the

significant reduction in inward currents with tropinone imply that heteromeric α3β4 receptors may play a more prominent role in ChCs' cholinergic modulation than α7. Notably, α4-containing nicotinic receptors, rather than α7, are essential for the normal development of ChC axonal arborization (Steinecke et al., 2022).

An important contribution of ChCs lies in their axo-axonic synapses at the AIS of PNs, one of the most powerful sites for modulating neuronal output (Howard et al., 2005; Kole and Stuart, 2012; Veres et al., 2014). By targeting the AIS, ChCs can either dampen or synchronize pyramidal cell firing (Isaacson and Scanziani, 2011; Meyer et al., 2011; Roux and Buzsáki, 2015). Our findings refine this perspective by demonstrating that, during high-arousal states, cholinergic tone can powerfully excite ChCs via nAChRs. This phenomenon could shift the balance of local inhibition in favor of more precise or temporally locked inhibition at the AIS, thereby gating pyramidal cell firing during behaviors that require heightened attention or rapid sensorimotor integration (Fu et al., 2014; McGinley et al., 2015a, 2015b; Vinck et al., 2015). Remarkably, ChCs exhibit heightened activity during locomotion across various brain regions, including the hippocampus, visual cortex, and M2 (Dudok et al., 2021; Jung et al., 2023; Schneider-Mizell et al., 2021; Seignette et al., 2024). In the visual cortex, ChCs show a clear relationship between their activity and pupil dilation during locomotion, further supporting their preferential activation during high-arousal states (Schneider-Mizell et al., 2021; Seignette et al., 2024). However, in M2, prior study has primarily emphasized the link between ChC activity and locomotion (Jung et al., 2023). Here, we extend these findings by demonstrating that M2 ChCs also correlate strongly with pupil dilation, an established proxy for neuromodulatory activity and arousal. Our results revealed that M2 ChCs exhibit positive correlations with locomotion and pupil fluctuations during behavioral quiescence. These data indicate that M2 ChCs are

sensitive to changes in arousal levels and not solely to motor output. This aligns with the broader consensus that cholinergic input is central to shifting cortical network states from quiet wakefulness to active behaviors, as ACh is strongly linked to high-arousal states, which are reflected in pupil dynamics (McGinley et al., 2015b; Neyhart et al., 2024; Reimer et al., 2016).

Moreover, the capacity of ChCs to respond directly to nicotinic inputs suggests that these interneurons can be quickly and strongly recruited during behavioral states requiring rapid cortical engagement. The BF, which provides the principal source of cortical cholinergic innervation, dynamically adjusts cortical excitability as animals transition from rest to active behaviors (Ananth et al., 2023; Ballinger et al., 2016; Gielow and Zaborszky, 2017). Our optogenetic experiments confirm that these projections form functional contacts with ChCs in M2. Because M2 is implicated in motor planning and action selection (Jung et al., 2023, 2022; Yang and Kwan, 2021), it is plausible that cholinergic excitation of ChCs refines cortical output during behaviors reliant on precise temporal coordination, such as locomotion or decision making (McGinley et al., 2015a, 2015b; Vinck et al., 2015).

While our study offers robust evidence for the cholinergic regulation of chandelier cells, several critical questions remain unresolved. First, although we identified key subunits of nicotinic acetylcholine receptors, the precise role of α3 subunits and other less common subunits demands further investigation to clarify receptor composition and kinetics fully. Second, although the in vivo nicotinic blockade establishes a causal link between nicotinic signaling and changes in ChC engagement, this approach impacts not only ChCs but also other cell types expressing nAChRs, which may, in turn, influence ChCs through synaptic interactions. Therefore, more precise manipulations targeting nicotinic inputs specifically to ChCs are needed. Third, ChCs might integrate

inputs from additional neuromodulatory systems, including noradrenergic or serotonergic pathways. Investigating these pathways will be crucial to constructing a comprehensive model of ChC function in both normal and pathological conditions. Finally, while we have examined the impact of cholinergic blockade on ChC activity, it is crucial to assess how this blockade affects the broader cortical circuit. A recent study demonstrated the role of M2 cortical ChCs in facilitating efficient cortical computation in a cell-specific manner(Jung et al., 2023). Notably, chemogenetic inhibition of ChCs led to increased co-activity of M2 neurons during locomotion. Given that cholinergic blockade reduces ChC activity during movement, it is plausible that alterations in nicotinic modulation could disrupt the proper functioning of the cortical network.

In summary, our results reveal that ChCs in M2 are subject to pronounced and direct cholinergic modulation via β2- and α3-containing nAChRs. This neuromodulatory influence aligns with high-arousal states, reinforcing the notion that ChCs act as an integrative hub where local cortical architecture converges with global signals from the BF. By linking state-dependent changes in cholinergic tone to the specialized inhibition at the AIS, our findings underscore ChCs potential to dynamically regulate cortical output at behaviorally relevant timescales. Future studies aimed at dissecting the full spectrum of neuromodulatory control over ChCs will undoubtedly refine our understanding of how these interneurons contribute to circuit-level computations and behavior.

Methods

All procedures related with animal investigation were performed in accordance with the European Union Directive 2010/63/EU and Spanish law (R.D. 53/2013 BOE 34/11370-420, 2013) for the use and care of laboratory animals and approved by the

competent Spanish entity ("Consejería de agricultura, pesca y desarrollo rural. Dirección general de la producción agrícola y ganadera") with authorized project number 16/12/2020/146. All mice were maintained in the university animal facility (Centro de Experimentación Animal Óscar Pintado) of the Centro de Investigación, Tecnología e Innovación de la Universidad de Sevilla (CITIUS) on a 12h-light/12h-dark cycle e and housed in standard cages with unrestricted access to food and water.

Animals

Both male and female mices (~2 months old) were used for all experiments. The following transgenic lines were obtained from The Jackson Laboratory: *Vipr2*^{Cre} (strain 031332), *Pvalb*^{Flp} (strain 022730), *Ai65D* (strain 021875) and *Chat*^{Cre} (strain 006410), *PV*^{Cre} (strain 008069) and *Ai14* (strain 007914). To genetically label ChCs with a tdTomato reporter, *Vipr2*^{Cre}:*Pvalb*^{Flp} mice were crossed with *Ai65D*, following the breeding strategy described by Tasic et al., 2018, generating the *VipR2-Pvalb-Ai65D* mouse line. To compare ChCs with parvalbumin-expressing cells, *PV*^{Cre} and *Ai14* mice were crossed to generate the PvCre-*Ai14* mouse line. Finally, in optogenetic experiments aimed at targeting cholinergic cells with ChR2, a quadruple transgenic line (*VipR2-Pvalb-Ai65D-ChAT*) was generated by crossing *Vipr2*^{Cre}:*Pvalb*^{Flp} mice and *Ai65D-Chat*^{Cre} mice. Genotyping was performed using PCR and according to supplier protocols. All experimental mice were heterozygous for their respective transgenes.

Tissue fixation and slices preparation

Mice were deeply anesthetized with 2% tribromoethanol (0.15 ml / 10 mg) and then transcardially perfused with 0.9% saline solution, followed by 4% paraformaldehyde (PFA) in 0.1 M phosphate buffer (PB, pH 7.4). The brains were removed, post-fixed in 4% PFA overnight at 4ºC, and then cryoprotected in 30% sucrose in PB containing

0.01% sodium azide until sectioning. Brains were subsequently frozen with O.C.T. compound (Tissue Tek) and then serially sectioned on a cryostat (Leica CM1950) into 40 µm-thick coronal slices. These slices were stored at -20ºC in 50% glycerol in phosphate buffered saline (PBS, pH 7.4). In some experiments (Figures 3 & 4), following electrophysiology, 300 µm-thick slices were fixed in 4% PFA overnight at 4°C, then cryoprotected and resectioned into 40 µm-thick coronal slices.

Immunofluorescence

Free-floating brain slices were washed with PBS and then blocked with 3% normal serum and 0.3% Triton X-100 in PBS for 45-60 min. Next, slices were incubated overnight at 4ºC with primary antibodies in the same blocking solution. After washing with PBS, slices were incubated for 2 hours at room temperature with appropriate secondary antibodies (Goat or Donkey Alexa Fluor 488, 647 or Rhodamine Red-X; 1:500, Jackson Immunoresearch) diluted in 1.5% normal donkey serum and 0.3% Triton X-100 in PBS. Finally, slices were washed and mounted on slides using FluorSafe Reagent (Cat#: 345789, Merk Millipore). The primary antibodies used were chicken CPCA-mCherry (1:1000, EnCor Bio, Cat#: CPCA-mCherry), rabbit Anti-parvalbumin (1:1000, Swant, Cat#: PV27), mouse Anti-parvalbumin (1:1000, Swant, Cat#: PV235), rabbit Anti-Phospho-IκBα (1:1000, Cell Signaling Technology, Cat#: 2859), goat Anti-ChAT (1:500, MerckMillipore, Cat#: AB114P), rabbit Anti-GFP (1:500, Synaptic Systems, Cat#: 132002) and chicken Anti-GFP (1:1000, Aves Labs, Cat#: #GFP-1010). An antigen-retrieval protocol was performed for experiments involving the goat anti-ChAT antibody before immunofluorescence. Briefly, slices were washed with PBS and incubated in sodium citrate solution (pH 6.0; Sigma) at 80°C in a water bath for 30 min. After rinsing with PBS, slices were blocked with 2% nonfat milk and 0.3% Triton X-100 in PBS for 30 min. Following another rinse, slices were blocked

again in 3% normal serum and 0.3% Triton X-100 in PBS for 45–60 min, then incubated for 48 hr at 4°C with goat anti-ChAT. Finally, slices were incubated for 2 h at room temperature with the corresponding secondary antibodies and mounted on slides using FluorSafe Reagent.

Fluorescent *in situ* RNA hybridization

Brains were obtained as described in *Tissue fixation and slices preparation*. They were then frozen with O.C.T. compound and serially sectioned on a cryostat (Leica CM1950) into 10 µm-thick coronal slices. Sections were mounted on SuperFrost Plus adhesion slides (J1800AMNZ, Epredia) and stored at -80ºC until use. The *in situ* hybridization was performed using the ViewRNA kit (ViewRNA technology, Invitrogen, ThermoFisher Scientific, QVT4600C) for fixed frozen tissue, following the manufacturer's instructions. All incubations were performed using an ACD HybEZ II Hybridation System. To minimize tissue damage, slides were gradually warmed from -20°C to 4°C and then to room temperature. A hydrophobic barrier was drawn around the sections with a hydrophobic pen (ImmEdge). Target probes used were Chrna3 (ID #VF6-10407-VC), Chrna7 (ID #VB6-3198060-VT) and Chrnb2 (ID #VB6-19634-VT). Negative (VF6-10407-VC) and positive (Actb, VB6-12823-VT) control probes provided in the kit were also used. A type 6 label probe (Alexa Fluor 647, Cy5 fluorochrome) was used for detection, and DAPI was added in the final steps to stain nuclei. To enhance the identification of ChCs, an immunofluorescence protocol against tdTomato using mCherry-CPCA was performed as previously described.

AAV design and production

For cloning of AAV-hSynP-Flex-Tdtomato, each component expression cassette (human Synapsin Promoter–LoxP–tdTomato–LoxP) was amplified individually using custom-designed primers. The fragments were then assembled via overlapping PCR using Q5 High-Fidelity DNA Polymerase (M0491S, New England Biolabs). The resulting product was cloned into a pre-existing adeno-associated virus (AAV) vector containing ITRs (#18916, Addgene) at the NdeI and HindIII restriction sites. Enzymes and reagents included NdeI (R0111S), HindIII (R3104S), DpnI (R0176L), Antarctic Phosphatase (M0289), and T4 DNA Ligase (M0202S) (all from New England Biolabs).

AAV vector production was performed by the Viral Vector Unit at CNIC. For encapsulation of tdTomato, the plasmid pUCmini-iCAP-PHP.eB (plasmid #103005, Addgene) was employed to provide the PHP.eB capsid. Viral titers were quantified by qPCR using primers targeting the woodchuck hepatitis virus post-transcriptional regulatory element (WPRE).

Acquisition and image analysis

Confocal imaging was performed on a Nikon A1R+ microscope with a 40x air objective lens or 20x and 60x glycerol immersion objectives (Nikon), depending on the experiment. For RNA hybridization studies, confocal images were acquired using a Leica Stellaris 9 microscope, employing a 20x glycerol immersion objective lens (Leica) and 3x digital magnification. All images presented in the figures were acquired via confocal microscopy, except for those in Figures 4 and 5, which were obtained using a two-photon microscope. Image analysis was conducted in Fiji software (Schindelin et al., 2012), with the experimenter blinded to the genotype to ensure unbiased data processing.

IMARIS analysis

The images were analyzed using IMARIS 9.6 software (Oxford Instruments) to reconstruct Chandelier cells (ChCs) based on tdTomato labeling and the axon initial segments (AIS) of pyramidal cells using p-IkBa immunofluorescence. Confocal images were acquired using a 20x objective to capture complete images of individual, isolated ChCs, facilitated by their relatively low abundance. The Filament Tracer tool was employed to reconstruct the axonal and dendritic branches of tdTomato^{+} ChCs. To perform three-dimensional reconstructions of ChC cartridges and pyramidal AIS, confocal images were obtained using a 60x objective, and the Surfaces-Surfaces contact tool was applied (available in: https://imaris.oxinst.com/open/view/surface-surface-contact-area). Briefly, the analysis quantifies contact surfaces within defined regions of interest (ROIs), ensuring consistency in volume between images. Manual selection of proximal and distal ROIs targeted AIS rods and ChCs cartridges. Segmentation parameters, such as a maximum diameter of 0.6 µm for the green channel, and manual thresholding ensured accurate representation of structures. Using the Surface-Surface Contact tool, AIS rods (primary surface) and cartridges (secondary surface) were analyzed to determine their overlap, visualized as a voxel-thick unsmoothed surface above the primary structure.

Stereotactic viral infection and window implantation

Stereotactic AAV injections

Two-month-old mice were anesthetized with isoflurane (5% for induction, 1.5-2% for maintenance in oxygen) delivered at a constant flow rate. The scalp was shaved, and carprofen (0.5 mg/mL), a nonsteroidal anti-inflammatory drug, was administered subcutaneously prior to surgery. Mice were then placed on a motorized stereotaxic frame (World Precision Instruments), and ophthalmic ointment was applied to prevent

corneal drying. The body temperature was maintained at 37°C using a thermostatically controlled heating pad (Physitemp TCAT-2LV). The scalp was disinfected with betadine and 70% ethanol, and an incision was made to expose the skull. After cleaning the skull with cortex buffer (NaCl 125 mM, Glucose 10 mM, KCl 5 mM, HEPES 10 mM, MgSO4 2 mM, CaCl2 2mM), the stereotactic coordinates were marked.

For viral injections targeting L2/3 of the M2 cortex, a small burr hole was drilled at the following coordinates (relative to bregma): anteroposterior (A/P) +2.8 mm, mediolateral (M/L) +1 mm, dorsoventral (D/V) −0.25 mm from the brain surface. For basal forebrain (BF) injections, three target areas were used: the nucleus of the vertical limb of the diagonal band (VDB; A/P +0.8 mm, M/L +0.5 mm, D/V −4.5 mm), the nucleus of the horizontal limb of the diagonal band (HDB; A/P 0 mm, M/L +1.5 mm, D/V −5.1 mm), and the nucleus basalis of Meynert/substantia innominata (NBM/SI; A/P −0.35 mm, M/L +1.6 mm, D/V −4.55 mm). The following viruses were injected as indicated in the figures: hSyn-tdTomato-FLEX or AAV1-EF1a-double-floxed-hChR2(H134R)-EYFP-WPRE (Addgene, Catalog #20298). The virus was loaded into a pulled glass micropipette, backfilled with mineral oil. The flow rate (5 nl/s) was controlled by a nanoinjector (Nanoject III, Drummond), delivering a total volume of 150-200 nl for M2 injections and 450 nl for each BF injection site. The pipette remained in place for 10 minutes before and after the injection to prevent backflow. The burr hole was sealed with silicon sealant (Kwik-cast, World Precision Instruments), and the incision was closed using skin adhesive (3M Vetbond). Mice were monitored until they recovered from anesthesia. For 3 days following surgery, mice received daily injections of carprofen (0.5 mg/ml).

Stereotactic AAV injections with cranial window

For the cranial window surgery, the scalp was removed after disinfection and cleaned with cortex buffer solution. The connective tissue was carefully excised with a scalpel to fully expose the skull, followed by the application of a thin layer of cyanoacrylate. The posterior portion of the skull was covered with black dental adhesive (Orthocryl, Dentaurum), and a custom-made headbar was affixed on top. A 2 mm diameter craniotomy was created around the M2 stereotactic coordinates to expose the underlying brain. The viral construct AAV1-Syn-Flex-GCaMP6s-WPRE-SV40 (Addgene, Catalog: #100845-AAV1) was injected as previously described.

To prepare the cranial window, a 3 mm diameter round glass cover (Warner Instruments, Cat#: 64-0720) was joined with a 1 mm diameter square glass cover (handmade with a diamond-tipped blade) using UV-curable optical adhesive (Thorlabs, NOA61). This assembled window was then implanted into the craniotomy and sealed with cyanoacrylate. The remaining skull surface was covered with dental adhesive. Mice were monitored until they recovered from anesthesia. For 3 days following the surgery, mice received daily injections of carprofen (0.5 mg/ml).

In vivo cholinergic blockade

Nicotinic antagonists (MMA and MLA) were dissolved in warm cortex buffer, filtered, and then injected into the cortex using a glass micropipette and a nanoinjector (Nanoject III, Drummond). During the initial surgery and AAV injection, a small hole was drilled through each coverslip intended for the cranial window. This hole was sealed with Kwik-Sil and covered with acrylic to prevent desiccation and infection.

Imaging sessions occurred three weeks after the AAV injection. The Kwik-Sil plug was removed, and GCaMP6-expressing ChCs were imaged for 8–10 minutes. Following this, the mouse was placed under a dissection microscope, where the glass

micropipette containing the filtered nicotinic antagonists was inserted into the cortex via the pre-drilled hole, preserving the integrity of the cranial window. After drug delivery, the mouse was repositioned under the two-photon microscope, the same neurons were located, and their activities were imaged again for another 8–10 minutes to assess the effects of the antagonists(Garcia-Junco-Clemente et al., 2019)

In vitro electrophysiology

Preparation of brain slices

Mice were anesthetized with 2% tribromoethanol (0.15 ml/10 mg) and decapitated. Brains were dissected-out and submerged in ice-cold cutting solution containing (in mM) 222 sucrose, 11 D-glucose, 3 KCl, 1 NaH_2PO_4, 26 mM $NaHCO_3$, 0.5 mM $CaCl_2$ and 7mM $MgCl_2$ (osmolality 305-315 mosmol/kg), pH 7.4, when bubbled with carbogen (5% CO2 - 95% O2). 300 µm thick coronal slices were cut using a Leica VT 1200S vibratome (Leica Biosystems, Wetzlar Germany). Slices were allowed to recover for 25 min at 35°C in artificial cerebrospinal fluid (ACSF) containing (in mM) 124 NaCl, 10 D-glucose, 2.5 KCl, 1.25 NaH_2PO_4, 26 mM $NaHCO_3$, 2.5 mM $CaCl_2$, 2mM $MgCl_2$ and 4 sucrose (osmolality 305-315 mosmol/kg), pH 7.4, when bubbled with carbogen (5% CO2 - 95% O2). They were subsequently kept at room temperature for 30-60 min before recording.

Electrophysiological recordings, data acquisition and analysis

Slices were transferred to a recording chamber installed in an upright microscope (Nikon Eclipse Ni-E). Recordings were carried out at 33 ±1Cº with continuous perfusion at a rate of 2-3 ml/min. Cells were visualized with a 40X water immersion objective lens (Nikon, NA 0.8, IR 40×/0.80 W) with infrared light source (Thorlabs, M940L3) and Dodt-Gradient-Contrast System (Luigs & Neumann) and a USB 3.0

monochrome camera (TheImagingSource, DMK 23U445). ChCs were identified as tdTomato$^+$ neurons using a high-power multi-LED (pE-300white, CoolLED). Whole-cell patch-clamp recordings were carried out using an EPC10 amplifier (HEKA). Patch pipettes were pulled from borosilicate glass (Science Products GmbH, Cat#: GB150F-8P) using a DMZ Universal Puller (Zeitz Instruments). After filling the pipettes with intracellular solution containing (in mM) 120 K-gluconate, 10 KCl, 10 phosphocreatine, 10 HEPES, 0.1 EGTA, 2 Mg-ATP, 0.3 Na_2-GTP (pH 7.25, 280-290 mosmol/kg) for all recordings, their resistances were 2.5-3.5 MΩ. Giga seals (>1GΩ) were always obtained before break-in. Throughout voltage-clamp recordings, whole-cell capacitance and series resistance were monitored, and series resistance was compensated by 70% (lag 10 μs). In all experiments, the neurons were discarded whether resistance increased more than 50% or exceeded 20 MΩ. For local application of 1,1-Dimethyl-4-phenyl piperazine iodide (DMPP), a glass pipette delivered a 20-ms, 4-psi puff to the dendritic region near the soma of ChCs, controlled by an Openspritzer (Forman et al., 2017). Bridge-balance and capacitances were fully compensated in current clamp recording.

Recordings were acquired using PatchMaster software (HEKA) with a low-pass filter at 2.9 kHz and digitized at 20 kHz. A D400 Multi-channel 50Hz/60Hz mains noise eliminator (Digitimer) was used. In current-clamp recordings, input resistance (Rin) was determined by injecting current pulses (10 pA increment, from –50 pA to +50 pA, 500 ms duration, 1 Hz) estimating the slope of the voltage-current plot. The membrane time constant (τ) was obtained by recording the membrane response to -50 pA current pulses (500 ms duration, 1 Hz) and fitting the averaged record of 10 sweeps to a single exponential curve. The rheobase was the minimum injected current (500 ms pulse duration at 1 Hz) to generate an action potential with 50% likelihood. Firing properties

were obtained during current injection steps (20 pA increments, 500 m) and represented as frequency-intensity (FI) plots. Action potential (AP) parameters were calculated from the rheobase recording. The AP threshold was calculated as the value of the membrane potential at which the first derivative surpassed 20 V/s. Recordings were analyzed with the software Stimfit (Guzman et al., 2014).

Optogenetic stimulation

To investigate BF cholinergic inputs to ChCs, we patched ChCs located in layer 2/3 of M2 that were surrounded by a high density of eYFP+ cholinergic axons. Optogenetic stimulation of BF cholinergic axons was delivered with 5 s pulses of blue light (2.5 mW/mm², 450 nm) using a high-power multi-LED system (pE-300white, CoolLED). Postsynaptic currents were recorded in voltage-clamp mode at a holding potential of −70 mV. To record monosynaptic transmission, we applied to the bath TTX (500 nM) to block action potential–dependent synaptic release and 4-aminopyridine (4-AP, 500 μM) to facilitate transmitter release from BF axons and thereby enhance the detectable response at monosynaptic connections (Cho et al., 2013).

Calcium signaling via two-photon imaging

Data collection and processing

Mice were head-fixed on a floating spherical treadmill, trained to balance and run during daily 20-minute sessions for five consecutive days before experimental procedures began. Imaging sessions were initiated 18–21 days post-AAV injection, upon confirmation of GCaMP6 expression in the M2 region. A resonant scanning two-photon microscope (Neurolabware, Los Angeles, CA) equipped with a pulsed Ti:sapphire laser (Chameleon Discovery, Coherent) and controlled by Scanbox acquisition software (Scanbox, Los Angeles, CA) was used for imaging. A 16x water

immersion objective (Nikon, 0.8 NA, 3 mm working distance) was employed at a zoom level of 1.4–1.7x. Laser excitation wavelengths were set to 920 nm for GCaMP6 signals and 1100 nm for tdTomato. The microscope operated at a frame rate of 15.6 Hz (512 lines using a resonant mirror at 8 kHz).

Imaging planes were chosen based on cell density and the extent of viral infection, targeting depths of 150–300 µm. GCaMP6 fluorescence signals were recorded for 8–10 minutes per plane, while tdTomato signals were captured over 30 seconds to facilitate post hoc identification of chandelier cells.

Experiments were conducted in the dark, illuminated with infrared light for visibility. Pupil size and ball movement were recorded concurrently using two cameras, each fitted with a 740 nm long-pass filter: a Dalsa M1280 at 30 fps for pupil monitoring and a Dalsa M640 at 60 fps for tracking ball movement. Both locomotion and eye movement data were synchronized with microscope frame acquisition. To pre-constrict the pupil, during the imaging session a small, non-dispersing light source was aimed at the contralateral eye.

Calcium imaging data were processed using MATLAB scripts provided by Scanbox, which included motion correction, segmentation, and signal extraction. Comparable results were achieved using the Suite2P pipeline (Pachitariu et al., 2017). MATLAB scripts from Scanbox were also used to analyze pupil signals and ball movement.

Data analysis

An analysis of calcium signals from ChCs, pupil dilation, and ball movement was performed using MATLAB. For the data in Figure 4, correlation coefficients were computed to assess the relationship between each ChC's activity and both locomotion and pupil diameter. GCaMP6s signals were classified as either tdTomato^{+} or

tdTomato$^-$ by aligning the tdTomato and GCaMP6 masks. For the data in Figure 5, a cross-correlation analysis was carried out to evaluate the relationship between motion and ChC activity. Additionally, changes in normalized amplitude were measured before and after the administration of nicotinic antagonists.

Statistical analysis

All statistical analysis was made using Past software (Hammer et al., 2021). The assessment of statistical significance was guided by tests for homogeneity of variance (Levene's test) and normality (Shapiro-Wilk test) applied to the compared samples. Depending on the distribution characteristics, statistical significance was determined using either Student's t-test or Mann-Whitney U test for pairwise comparisons. In situations where the datasets were paired, statistical significance was determined using paired Student's t-test or Wilcoxon signed-rank test. For repeated measures, we employed ANOVA followed by Tukey's post-hoc pairwise comparisons, or the Friedman test followed by Wilcoxon signed-rank tests with Bonferroni correction to identify specific differences between conditions. Box plots illustrate the 25th to 75th percentiles, represented by the box, with the median shown as a horizontal line within the box. Whiskers represent the minimum and maximum values.

Drugs and Solutions

All drugs and chemicals were from ThermoFisher Scientific (Waltham, MA), except for TTX (Latoxan Laboratory, France), CNQX, DL-AP5 and Picrotoxin (HelloBio, Princeton, NJ), MMA, DHβE and MLA (TOCRIS, UK) and Atropine and Tropinone (Sigma-Aldritch, St. Louis, MI).

References

Albuquerque EX, Pereira EFR, Alkondon M, Rogers SW. 2009. Mammalian Nicotinic Acetylcholine Receptors: From Structure to Function. doi:10.1152/physrev.00015.2008.-The

Ananth MR, Rajebhosale P, Kim R, Talmage DA, Role LW. 2023. Basal forebrain cholinergic signalling: development, connectivity and roles in cognition. *Nature Reviews Neuroscience 2023 24:4* **24**:233–251. doi:10.1038/s41583-023-00677-x

Arroyo S, Bennett C, Aziz D, Brown SP, Hestrin S. 2012. Prolonged Disynaptic Inhibition in the Cortex Mediated by Slow, Non-α7 Nicotinic Excitation of a Specific Subset of Cortical Interneurons. *Journal of Neuroscience* **32**:3859–3864. doi:10.1523/JNEUROSCI.0115-12.2012

Ballinger EC, Ananth M, Talmage DA, Role LW. 2016. Basal Forebrain Cholinergic Circuits and Signaling in Cognition and Cognitive Decline. *Neuron*. doi:10.1016/j.neuron.2016.09.006

Bloem B, Poorthuis RB, Mansvelder HD. 2014. Cholinergic modulation of the medial prefrontal cortex: The role of nicotinic receptors in attention and regulation of neuronal activity. *Front Neural Circuits*. doi:10.3389/fncir.2014.00017

Bugeon S, Duffield J, Dipoppa M, Ritoux A, Prankerd I, Nicoloutsopoulos D, Orme D, Shinn M, Peng H, Forrest H, Viduolyte A, Reddy CB, Isogai Y, Carandini M, Harris KD. 2022. A transcriptomic axis predicts state modulation of cortical interneurons. *Nature 2022 607:7918* **607**:330–338. doi:10.1038/s41586-022-04915-7

Cardin JA. 2018. Inhibitory Interneurons Regulate Temporal Precision and Correlations in Cortical Circuits. *Trends Neurosci*. doi:10.1016/j.tins.2018.07.015

Cecilia Gotti MZ and FC. 2006. Brain nicotinic acetylcholine receptors: native subtypes and their relevance. *Trends Pharmacol Sci*.

Cho JH, Deisseroth K, Bolshakov VY. 2013. Synaptic Encoding of Fear Extinction in mPFC-amygdala Circuits. *Neuron* **80**:1491–1507. doi:10.1016/J.NEURON.2013.09.025

Colangelo C, Shichkova P, Keller D, Markram H, Ramaswamy S. 2019. Cellular, synaptic and network effects of acetylcholine in the neocortex. *Front Neural Circuits* **13**:24. doi:10.3389/FNCIR.2019.00024/BIBTEX

Daigle TL, Madisen L, Hage TA, Valley MT, Knoblich U, Larsen RS, Takeno MM, Huang L, Gu H, Larsen R, Mills M, Bosma-Moody A, Siverts LA, Walker M, Graybuck LT, Yao Z, Fong O, Nguyen TN, Garren E, Lenz GH, Chavarha M, Pendergraft J, Harrington J, Hirokawa KE, Harris JA, Nicovich PR, McGraw MJ,

Ollerenshaw DR, Smith KA, Baker CA, Ting JT, Sunkin SM, Lecoq J, Lin MZ, Boyden ES, Murphy GJ, da Costa NM, Waters J, Li L, Tasic B, Zeng H. 2018. A Suite of Transgenic Driver and Reporter Mouse Lines with Enhanced Brain-Cell-Type Targeting and Functionality. *Cell* **174**:465-480.e22. doi:10.1016/J.CELL.2018.06.035

Dudok B, Szoboszlay M, Paul A, Klein PM, Liao Z, Hwaun E, Szabo GG, Geiller T, Vancura B, Wang B-S, McKenzie S, Homidan J, Klaver LMF, English DF, Huang ZJ, Buzsáki G, Losonczy A, Soltesz I. 2021. Recruitment and inhibitory action of hippocampal axo-axonic cells during behavior. *Neuron* 1–13. doi:10.1016/j.neuron.2021.09.033

Forman CJ, Tomes H, Mbobo B, Burman RJ, Jacobs M, Baden T, Raimondo J V. 2017. Openspritzer: an open hardware pressure ejection system for reliably delivering picolitre volumes. *Scientific Reports 2017 7:1* **7**:1–11. doi:10.1038/s41598-017-02301-2

Fu Y, Tucciarone JM, Espinosa JS, Sheng N, Darcy DP, Nicoll RA, Huang ZJ, Stryker MP. 2014. A Cortical Circuit for Gain Control by Behavioral State. *Cell* **156**:1139–1152. doi:10.1016/j.cell.2014.01.050

Garcia-Junco-Clemente P, Tring E, Ringach DL, Trachtenberg JT. 2019. State-Dependent Subnetworks of Parvalbumin-Expressing Interneurons in Neocortex. *Cell Rep* **26**:2282-2288.e3. doi:10.1016/j.celrep.2019.02.005

Gielow MR, Zaborszky L. 2017. The Input-Output Relationship of the Cholinergic Basal Forebrain. *Cell Rep* **18**:1817–1830. doi:10.1016/J.CELREP.2017.01.060

Guzman SJ, Schlögl A, Schmidt-Hieber C. 2014. Stimfit: Quantifying electrophysiological data with Python. *Front Neuroinform* **8**:71453. doi:10.3389/FNINF.2014.00016/ABSTRACT

Hammer Ø, Harper DA, Ryan PD. 2021. PAST: PALEONTOLOGICAL STATISTICS SOFTWARE PACKAGE FOR EDUCATION AND DATA ANALYSIS. *Palaeontologia Electronica* **4**:1–9.

Hangya B, Ranade SP, Lorenc M, Kepecs A. 2015. Central Cholinergic Neurons Are Rapidly Recruited by Reinforcement Feedback. *Cell* **162**:1155–1168. doi:10.1016/J.CELL.2015.07.057/ATTACHMENT/827D2264-3462-4EDB-BC46-BDA63310CA38/MMC2.PDF

Hasselmo ME, Sarter M. 2011. Modes and Models of Forebrain Cholinergic Neuromodulation of Cognition. *Neuropsychopharmacology* **36**:52–73. doi:10.1038/npp.2010.104

Howard A, Tamas G, Soltesz I. 2005. Lighting the chandelier: new vistas for axo-axonic cells. *Trends Neurosci* **28**:310–6. doi:10.1016/j.tins.2005.04.004

Inan M, Anderson SA. 2014. The chandelier cell, form and function. *Curr Opin Neurobiol*. doi:10.1016/j.conb.2014.01.009

Isaacson JS, Scanziani M. 2011. How inhibition shapes cortical activity. *Neuron* **72**:231–243. doi:10.1016/j.neuron.2011.09.027

Josh Huang Z, Paul A. 2019. The diversity of GABAergic neurons and neural communication elements, Nature Reviews Neuroscience. doi:10.1038/s41583-019-0195-4

Jung K, Chang M, Steinecke A, Burke B, Choi Y, Oisi Y, Fitzpatrick D, Taniguchi H, Kwon H-B. 2023. An adaptive behavioral control motif mediated by cortical axo-axonic inhibition. *Nature Neuroscience 2023* 1–15. doi:10.1038/s41593-023-01380-x

Jung K, Choi Y, Kwon HB. 2022. Cortical control of chandelier cells in neural codes. *Front Cell Neurosci* **16**:504. doi:10.3389/FNCEL.2022.992409/BIBTEX

Kole MHP, Stuart GJ. 2012. Signal Processing in the Axon Initial Segment. *Neuron* **73**:235–247. doi:10.1016/J.NEURON.2012.01.007/ASSET/71E6DEC6-B8DA-4245-874F-9743C9D9CEF0/MAIN.ASSETS/GR6.JPG

Krenz I, Kalkan D, Wevers A, De Vos RAI, Jansen Steur ENH, Lindstrom J, Pilz K, Nowacki S, Schütz U, Moser N, Witter B, Schröder H. 2001. Parvalbumin-containing interneurons of the human cerebral cortex express nicotinic acetylcholine receptor proteins. *J Chem Neuroanat* **21**:239–246. doi:10.1016/S0891-0618(01)00112-0

Lee SH, Dan Y. 2012. Neuromodulation of Brain States. *Neuron* **76**:209–222. doi:10.1016/J.NEURON.2012.09.012/ASSET/3DB19F9C-E09D-4B4E-8DC2-8D3D9174174D/MAIN.ASSETS/GR5.JPG

Lu J, Tucciarone J, Padilla-Coreano N, He M, Gordon JA, Huang ZJ. 2017. Selective inhibitory control of pyramidal neuron ensembles and cortical subnetworks by chandelier cells. *Nat Neurosci* **20**:1377–1383. doi:10.1038/nn.4624

Marín O. 2012. Interneuron dysfunction in psychiatric disorders. *Nat Rev Neurosci* **13**:107–120. doi:10.1038/nrn3155

McGinley MJ, David S V., McCormick DA. 2015a. Cortical Membrane Potential Signature of Optimal States for Sensory Signal Detection. *Neuron* **87**:179–192. doi:10.1016/J.NEURON.2015.05.038/ATTACHMENT/A016AD79-DDF2-4124-A61B-3F33E594AC6B/MMC3.PDF

McGinley MJ, Vinck M, Reimer J, Batista-Brito R, Zagha E, Cadwell CR, Tolias AS, Cardin JA, McCormick DA. 2015b. Waking State: Rapid Variations Modulate Neural and Behavioral Responses. *Neuron* **87**:1143–1161. doi:10.1016/J.NEURON.2015.09.012/ASSET/C5C41727-07E8-421F-AD20-9367B5C2B62D/MAIN.ASSETS/GR7.JPG

Mechawar N, Cozzari C, Descarries L. 2000. Cholinergic innervation in adult rat cerebral cortex: A quantitative immunocytochemical description. *J Comp Neurol* **428**:305–318. doi:10.1002/1096-9861(20001211)428:2<305::AID-CNE9>3.0.CO;2-Y

Meyer HS, Schwarz D, Wimmer VC, Schmitt AC, Kerr JND, Sakmann B, Helmstaedter M. 2011. Inhibitory interneurons in a cortical column form hot zones of inhibition in layers 2 and 5A. *Proceedings of the National Academy of Sciences* **108**:16807–16812. doi:10.1073/pnas.1113648108

Nakashima M, Ikegaya Y, Morikawa S. 2022. Genetic labeling of axo-axonic cells in the basolateral amygdala. *Neurosci Res*. doi:10.1016/j.neures.2022.02.002

Neyhart E, Zhou N, Munn BR, Mcginley MJ, Shine JM, Correspondence JR, Law RG, Smith C, Mridha ZH, Blanco FA, Li G, Li Y, Hu M, Reimer J. 2024. Cortical acetylcholine dynamics are predicted by cholinergic axon activity and behavior state. *Cell Rep* **43**:114808. doi:10.1016/J.CELREP.2024.114808

Pachitariu M, Stringer C, Dipoppa M, Schröder S, Rossi LF, Dalgleish H, Carandini M, Harris KD. 2017. Suite2p: beyond 10,000 neurons with standard two-photon microscopy. *bioRxiv* 061507. doi:10.1101/061507

Polack P-O, Friedman J, Golshani P. 2013. Cellular mechanisms of brain state–dependent gain modulation in visual cortex. *Nat Neurosci* **16**:1331–1339. doi:10.1038/nn.3464

Poorthuis RB, Bloem B, Schak B, Wester J, de Kock CPJ, Mansvelder HD. 2013. Layer-Specific Modulation of the Prefrontal Cortex by Nicotinic Acetylcholine Receptors. *Cerebral Cortex* **23**:148–161. doi:10.1093/cercor/bhr390

Porter JT, Cauli B, Tsuzuki K, Lambolez B, Rossier J, Audinat E. 1999. Selective excitation of subtypes of neocortical interneurons by nicotinic receptors. *Journal of Neuroscience* **19**:5228–5235. doi:10.1523/jneurosci.19-13-05228.1999

Povysheva N V., Zaitsev A V., Gonzalez-Burgos G, Lewis DA. 2013. Electrophysiological Heterogeneity of Fast-Spiking Interneurons: Chandelier versus Basket Cells. *PLoS One* **8**:e70553. doi:10.1371/journal.pone.0070553

Raudales R, Kim G, Kelly SM, Hatfield J, Guan W, Zhao S, Paul A, Qian Y, Li B, Huang ZJ. 2024. Specific and comprehensive genetic targeting reveals brain-wide distribution and synaptic input patterns of GABAergic axo-axonic interneurons. *Elife* **13**. doi:10.7554/eLife.93481

Reimer J, Froudarakis E, Cadwell CR, Yatsenko D, Denfield GH, Tolias AS. 2014. Pupil Fluctuations Track Fast Switching of Cortical States during Quiet Wakefulness. *Neuron* **84**:355–362. doi:10.1016/J.NEURON.2014.09.033

Reimer J, McGinley MJ, Liu Y, Rodenkirch C, Wang Q, McCormick DA, Tolias AS. 2016. Pupil fluctuations track rapid changes in adrenergic and cholinergic activity in cortex. *Nat Commun* **7**:13289. doi:10.1038/ncomms13289

Roux L, Buzsáki G. 2015. Tasks for inhibitory interneurons in intact brain circuits. *Neuropharmacology* **88**:10–23. doi:10.1016/J.NEUROPHARM.2014.09.011

Rudy B, Fishell G, Lee SH, Hjerling-Leffler J. 2010. Three groups of interneurons account for nearly 100% of neocortical GABAergic neurons. *Dev Neurobiol* **71**:45–61. doi:10.1002/dneu.20853

Rybnicek J, Chen Y, Milic M, Tio ES, McLaurin JA, Hohman TJ, De Jager PL, Schneider JA, Wang Y, Bennett DA, Tripathy S, Felsky D, Lambe EK. 2024. CHRNA5 links chandelier cells to severity of amyloid pathology in aging and Alzheimer's disease. *Translational Psychiatry 2024 14:1* **14**:1–13. doi:10.1038/s41398-024-02785-3

Schindelin J, Arganda-Carreras I, Frise E, Kaynig V, Longair M, Pietzsch T, Preibisch S, Rueden C, Saalfeld S, Schmid B, Tinevez JY, White DJ, Hartenstein V, Eliceiri K, Tomancak P, Cardona A. 2012. Fiji: an open-source platform for biological-image analysis. *Nature Methods 2012 9:7* **9**:676–682. doi:10.1038/nmeth.2019

Schneider-Mizell CM, Bodor AL, Collman F, Brittain D, Bleckert A, Dorkenwald S, Turner NL, Macrina T, Lee K, Lu R, Wu J, Zhuang J, Nandi A, Hu B, Buchanan J, Takeno MM, Torres R, Mahalingam G, Bumbarger DJ, Li Y, Chartrand T, Kemnitz N, Silversmith WM, Ih D, Zung J, Zlateski A, Tartavull I, Popovych S, Wong W, Castro M, Jordan CS, Froudarakis E, Becker L, Suckow S, Reimer J, Tolias AS, Anastassiou CA, Seung HS, Reid RC, Costa NM da. 2021. Structure and function of axo-axonic inhibition. *Elife* **10**. doi:10.7554/ELIFE.73783

Schultz C, König HG, Del Turco D, Politi C, Eckert GP, Ghebremedhin E, Prehn JHM, Kögel D, Deller T. 2006. Coincident enrichment of phosphorylated IκBα, activated IKK, and phosphorylated p65 in the axon initial segment of neurons. *Molecular and Cellular Neuroscience* **33**:68–80. doi:10.1016/j.mcn.2006.06.008

Seignette K, Jamann N, Papale P, Terra H, Porneso RO, de Kraker L, van der Togt C, van der Aa M, Neering P, Ruimschotel E, Roelfsema PR, Montijn JS, Self MW, Kole MHP, Levelt CN. 2024. Experience shapes chandelier cell function and structure in the visual cortex. *Elife* **12**. doi:10.7554/eLife.91153

Somogyi P. 1977. A specific 'axo-axonal' interneuron in the visual cortex of the rat. *Brain Res* **136**:345–350. doi:10.1016/0006-8993(77)90808-3

Steinecke A, Bolton MM, Taniguchi H. 2022. Neuromodulatory control of inhibitory network arborization in the developing postnatal neocortex. *Sci Adv* **8**. doi:10.1126/SCIADV.ABE7192

Taniguchi H, Lu J, Huang ZJ. 2013. The spatial and temporal origin of chandelier cells in mouse neocortex. *Science* **339**:70–4. doi:10.1126/science.1227622

Tasic B, Yao Z, Graybuck LT, Smith KA, Nguyen TN, Bertagnolli D, Goldy J, Garren E, Economo MN, Viswanathan S, Penn O, Bakken T, Menon V, Miller J, Fong O, Hirokawa KE, Lathia K, Rimorin C, Tieu M, Larsen R, Casper T, Barkan E, Kroll M, Parry S, Shapovalova N V., Hirschstein D, Pendergraft J, Sullivan HA, Kim TK, Szafer A, Dee N, Groblewski P, Wickersham I, Cetin A, Harris JA, Levi BP, Sunkin SM, Madisen L, Daigle TL, Looger L, Bernard A, Phillips J, Lein E, Hawrylycz M, Svoboda K, Jones AR, Koch C, Zeng H. 2018. Shared and distinct transcriptomic cell types across neocortical areas. *Nature* **563**:72–78. doi:10.1038/s41586-018-0654-5

Tremblay R, Lee S, Rudy B. 2016. GABAergic Interneurons in the Neocortex: From Cellular Properties to Circuits. *Neuron* **91**:260–292. doi:10.1016/j.neuron.2016.06.033

Veres JM, Nagy GA, Vereczki VK, Andrási T, Hájos N. 2014. Strategically Positioned Inhibitory Synapses of Axo-axonic Cells Potently Control Principal Neuron Spiking in the Basolateral Amygdala. *Journal of Neuroscience* **34**:16194–16206. doi:10.1523/JNEUROSCI.2232-14.2014

Vinck M, Batista-Brito R, Knoblich U, Cardin JA. 2015. Arousal and Locomotion Make Distinct Contributions to Cortical Activity Patterns and Visual Encoding. *Neuron* **86**:740–754. doi:10.1016/J.NEURON.2015.03.028/ATTACHMENT/3D3D705C-EF75-4293-B1AC-56F08B84999C/MMC4.PDF

Wang X, Tucciarone J, Jiang S, Yin F, Wang BS, Wang D, Jia Y, Jia X, Li Y, Yang T, Xu Z, Akram MA, Wang Y, Zeng S, Ascoli GA, Mitra P, Gong H, Luo Q, Huang ZJ. 2019. Genetic Single Neuron Anatomy Reveals Fine Granularity of Cortical Axo-Axonic Cells. *Cell Rep* **26**:3145-3159.e5. doi:10.1016/J.CELREP.2019.02.040/ATTACHMENT/987709D2-5465-421A-9856-CA29147D58D9/MMC8.PDF

Woodruff A, Xu Q, Anderson SA, Yuste R. 2009. Depolarizing effect of neocortical chandelier neurons. *Front Neural Circuits* **3**:15. doi:10.3389/neuro.04.015.2009

Woodruff AR, McGarry LM, Vogels TP, Inan M, Anderson SA, Yuste R. 2011. State-Dependent Function of Neocortical Chandelier Cells. *Journal of Neuroscience* **31**:17872–17886. doi:10.1523/JNEUROSCI.3894-11.2011

Xu X, Callaway EM. 2009. Laminar Specificity of Functional Input to Distinct Types of Inhibitory Cortical Neurons. *The Journal of Neuroscience* **29**:70–85. doi:10.1523/JNEUROSCI.4104-08.2009

Yang JH, Kwan AC. 2021. Secondary motor cortex: Broadcasting and biasing animal's decisions through long-range circuitsInternational Review of

Neurobiology. Academic Press Inc. pp. 443–470.
doi:10.1016/bs.irn.2020.11.008

Acknowledgements

We gratefully acknowledge the support and advice provided by R. Fernández-Chacón, the help with Imaris software to Nozha Borjini, the excellent technical assistance of C. Cabrera-Romero and G. Asensio Gómez, and the technical support of the staff at IBiS and the Centro de Investigación, Tecnología e Innovación de la Universidad de Sevilla (CITIUS). This project was supported by: grant PGC2018-095656-B-I00 funded by MICIU/AEI/10.13039/501100011033 (PGJC and JLNG) and by ERDF "A way of making Europe", grant PID2021-123840NB-I00 funded by MICIU/AEI/10.13039/501100011033 and by "ERDF/EU" (PGJC and JLNG), grant US-1264432 funded by US/JUNTA/FEDER, UE (PGJC and JLNG), grant RyC-2016-19906 (PGJC) and PRE2019-087729 (EMM) funded by MICIU/AEI/10.13039/501100011033 and by "ESF Investing in your future", grant RyC-2016-19906 funded by VI PPIT-US and grant PREDOC_00594 funded by Junta de Andalucía (SRL).

Author contributions

Emilio Martinez-Marquez, data collection, data analysis, reviewing/editing; Santiago Reyes-Leon, data collection, data analysis, writing, reviewing/editing; Flores García-Sanjosé, data collection and data analysis, Santiago López-Begines, methodology; Pablo Garcia-Junco Clemente and Jose L. Nieto-Gonzalez, conceptualization, experimental design, data collection, interpretation, writing, review/editing and funding.

Competing interests: Authors declare that they have no competing interests.

Figures and figure legends

Figure 1. Characterization of chandelier cells in VipR2-Pvalb-Ai65 mice.

(A) Low-magnification confocal image of a coronal neocortical section showing tdTomato$^+$ cells (magenta) in L1 and 2/3. White dashed lines mark the border between L1 and L2/3; arrows point to representative tdTomato-expressing cell bodies.

(B) Higher-magnification view of a tdTomato$^+$ cell in L2/3 that extend dendrites into L1 (left). The panel on the right shows morphological reconstructions (orange) of the same cell.

(C) Image of tdTomato (magenta) and PIkB (green) immunostaining, a marker for the AIS, in L2/3. Note vertical "cartridge" arrays characteristic of ChCs. The dashed boxes outline regions shown at higher magnification in (D)

(D) High-magnification views of AIS-innervating ChC cartridges (magenta) adjacent to PIkB AIS segments (green). Magnified views of tdTomato-expressing processes (magenta) and PIkB immunoreactivity (green), revealing close appositions. Below, a merged insert shows morphological reconstructions of the two channels superimposed. **(E)** Representative quantifications are shown as box plots.

(F) Representative confocal image illustrating tdTomato$^+$ cells (magenta) and parvalbumin (green) immunostaining in L1–L2/3. Dashed boxes mark regions enlarged in (G) and (H).

(G, H) Enlarged views of tdTomato$^+$ cells exhibiting the classic ChC morphology with vertically oriented dendritic trees and axonal cartridges. Parvalbumin$^+$ cells (green) are visible nearby.

(I) Quantification of parvalbumin and tdTomato co-localization (green bars): ~90% of parvalbumin$^+$ neurons are tdTomato$^-$, while ~80% of tdTomato$^+$ cells co-express

parvalbumin, indicating that ChCs represent a minority subpopulation of parvalbumin interneurons.

(J) Example fluorescence-guided patch-clamp recording of a tdTomato+ cell (arrow) at the L1–L2/3 boundary. The recording pipette tip is visible in pseudocolor blue.

(K) Electrophysiological responses recorded from tdTomato+ neurons. Left: example of a subthreshold membrane response to current injection. Middle: suprathreshold firing in response to a depolarizing current injection. Right: raster plot summarizing the firing patterns across multiple depolarizing current injections. Each dot represents a single action potential event.

Figure 2. Heteromeric nicotinic receptors mediate the cholinergic response in chandelier cells.

(A) Left, schematic of the experimental setup illustrating a tdTomato$^+$ ChC targeted for whole-cell patch-clamp recording while DMPP (a nicotinic agonist) is pressure-ejected. Right, representative infrared micrograph showing the ChC approached by both the recording and delivering pipette.

(B) Whole-cell patch-clamp recordings illustrating nAChRs contribution to DMPP-evoked inward currents in ChCs. Grey trace represents response under control conditions, red trace under synaptic transmission blockade (TTX, 1 μM; atropine, 1 μM; CNQX, 10 μM; picrotoxin, 50 μM; AP-V, 50 μM), and blue trace after subsequent application of mecamylamine (MMA, 5 μM), a pan nAChR antagonist. (**$p < 0.01$, Wilcoxon signed-rank test).

(C–E) Fluorescent in situ hybridization of nicotinic receptor subunits in tdTomato-labeled ChCs. White dashed outlines indicate soma boundaries. (C) CHRNB2 (magenta) is detected in the majority of ChCs (73.78% of cells). (D) CHRNA7

(magenta) is present in a smaller subset (17.86%). (E) CHRNA3 (magenta) is observed in nearly 30% of ChCs.

(F–I) Whole-cell patch-clamp recordings illustrating subunit-specific contributions to DMPP-evoked inward currents in ChCs. Grey traces represent responses under control conditions, red traces under synaptic transmission blockade (TTX, 1 μM; atropine, 1 μM; CNQX, 10 μM; picrotoxin, 50 μM; AP-V, 50 μM), and blue traces after subsequent application of the indicated nicotinic antagonists: (F) the β2-selective antagonist DHβE (10 μM), (G) the α7 antagonist methyllycaconitine (MLA, 200 nM), (H) sequential application of DHβE and MLA, and (I) the α3-selective antagonist tropinone (300 μM) following DHβE. The box plots on the right summarize the peak amplitudes measured under each experimental condition. (**$p < 0.01$, ***$p < 0.001$, Friedman test with Wilcoxon test (Bonferroni correction) (F, H, I), ANOVA with Tukey's post-hoc test (G)).

Figure 3. Optogenetic stimulation of basal forebrain cholinergic axons evoke an inward current in Chandelier Cells

(A–C) Top panels: Schematic illustrations (insert) indicate three rostro-caudal levels of the injections site (see methods for exact coordinates). Large panels show low-magnification views of YFP (green) and tdTomato (red) expression overlaid with immunostaining for choline acetyltransferase (ChAT; magenta). Major forebrain structures are outlined, including cortex, striatum, and lateral ventricles (LV), as indicated. Boxed regions in each low-magnification image are enlarged below. Below panels: representative images of the vertical diagonal band (VDB), horizontal diagonal band (HDB), and nucleus basalis of Meynert /substantia innominata (NBM/SI) reveal

dense cholinergic fiber innervation. Yellow arrows highlight examples of doubly labeled cells for YFP and ChAT.

(D) High-magnification confocal images of cortical cholinergic terminals illustrate co-localization of YFP (green), tdTomato (red), and ChAT (magenta). The boxed area in the left panel is shown at higher resolution on the right; yellow arrows indicate cholinergic varicosities labeled by all three markers. Insert schematizes the experimental setup, with an electrode recording from a cortical neuron (L2/3) receiving BF cholinergic projections expressing ChR2.

(E) Whole-cell patch-clamp recordings showing light evoked postsynaptic currents. Grey traces represent responses under control conditions, red traces under synaptic transmission blockade (TTX, 1 μM; atropine, 1 μM; CNQX, 10 μM; picrotoxin, 50 μM; AP-V, 50 μM), and blue traces after subsequent application of the nicotinic antagonists DHβE (10 μM), methyllycaconitine (MLA, 200 nM) and of mecamylamine (MMA, 5 μM).

(F) The box plots summarize the peak amplitudes measured under each experimental condition.

Figure 4. Chandelier cell activity in M2 cortex correlates with high-arousal behavioral states.

(A) Schematic overview of the experimental approach. Adult *VipR2-Cre+/-; PvalbFlp+/-; Ai65+/-* mice were injected in M2 cortex with a Cre-dependent AAV expressing GCaMP6s. During two-photon calcium imaging, head-fixed mice navigated on a floating spherical treadmill, and pupil diameter and running speed were recorded simultaneously.

(B) Representative two-photon images from layer 2/3 of M2 showing co-expression of GCaMP6 (green) and tdTomato (magenta). Some cells (white arrowheads) express both tdTomato and GCaMP6, whereas others express GCaMP6 alone (white arrows). Right, zoomed view of a single GCaMP6-labeled ChC soma (white arrow) and axonal cartridges (yellow arrow).

(C) Immunohistochemical confirmation of ChC identity. GCaMP6 (green) labels neuronal processes with the characteristic ChC “cartridge” morphology (middle and right), whereas immunostaining for parvalbumin (magenta) identifies parvalbumin$^+$ interneurons (left). Dashed boxes highlight regions shown at higher magnification. Bar graphs (far right) indicate the proportion of parvalbumin-labeled cells (left bar) that are GCaMP6$^+$ (light green) versus GCaMP6$^+$ (dark green) and the proportion of GCaMP6-labeled cells (right bar) that are parvalbumin$^+$ (dark green) versus GCaMP6$^-$ (light green).

(D) Representative activity heat map illustrating calcium events (in GCaMP6-labeled ChCs) over time. The red trace at the top represents the animal's running behavior throughout the corresponding time course.

(E) Scatter plot of correlation coefficients for individual ChCs (filled circles denote tdTomato$^+$ cells; circles denote tdTomato$^-$ cells).

(F) Histograms of correlation coefficients for running (red) and pupil diameter (blue) of tdTomato$^+$ cells and tdTomato$^-$ cells.

(G) Bar plot showing the correlation index between running and ChC signal (red) and pupil diameter and ChC signal (blue) (mean ± SEM). (**$p < 0.01$, Mann-Whitney U test)

(H) Representative time series from a single imaging session demonstrating that ChC calcium signals (gray) track running bouts (red) and spontaneous pupil fluctuations (blue).

Figure 5. Blockade of nicotinic receptors reduces running-evoked chandelier cell calcium signals.

(A) Example traces showing the mean calcium signal from ChCs (gray) aligned with running behavior (red). The top trace represents control conditions, while the bottom trace illustrates the effects after bath application of the nicotinic receptor antagonists mecamylamine (MMA) and methyllycaconitine (MLA). The right panels display pseudocolor fluorescence images of ChC somata and processes within the field of view corresponding to the recordings on the left. The top image represents control conditions, while the bottom image demonstrates reduced fluorescence following the application of MMA and MLA.

(B) Left: Cross-correlation analysis of ChC calcium responses and running behavior under control conditions and after local infusion of the nicotinic receptor antagonists MMA and MLA (mean ± SEM). Right: Zero-time cross-correlation values of ChCs under these conditions (***$p < 0.001$, Wilcoxon signed-rank test).

(C) Left: Average running-associated calcium transient responses under control (blue) and MMA+MLA (red) conditions (mean ± SEM). The vertical dashed line indicates the onset of running. Right: Box plots showing the quantification of normalized calcium transient amplitudes during stop and run states under control (blue) and MMA+MLA (red) conditions (***$p < 0.001$, ANOVA with Tukey's post hoc test).

Figure 1—figure supplement 1. Electrophysiological comparison between chandelier cells and basket cells.

(A–C) Electrophysiological responses recorded from chandelier cells (ChCs) in VipR2-Pvalb-Ai65D mice and basket cells (BCs) in PvCre-Ai14 mice.

(A) Example of a subthreshold membrane response to a current injection used to measure the membrane time constant (Tau).

(B) Example of a subthreshold membrane response to different current injections used to measure input resistance (Rin).

(C) Representative traces illustrating increased firing frequency with increasing injected current (F/I).

(D) Frequency–intensity (F/I) plot for ChCs (red) and BCs (blue) showing quantification of neuronal firing in response to incremental current injections.

(E) Boxplots summarizing intrinsic and action potential properties of ChCs (red) and BCs (blue), ***$p < 0.001$, unpaired t-test.

Figure 2 – figure supplement 1. Direct modulation of chandelier cells by nicotinic acetylcholine receptors.

(A) Whole-cell patch-clamp recordings of Chandelier Cells (ChCs) in the M2 cortex reveal a reversible depolarization of the resting membrane potential following bath application of the cholinergic agonist carbachol (25 μM) in the presence of TTX (1 μM). The accompanying box plot quantifies the depolarization response and subsequent washout phase (***$p < 0.001$, ANOVA with Tukey's post hoc test).

(B) Similar depolarization is observed with the nicotinic agonist DMPP (25 μM), indicating the involvement of nAChRs. Box plot showing the depolarization response

and washout phase, with significant changes observed (***$p < 0.001$, Friedman test with Wilcoxon test (Bonferroni correction)).

(C) The depolarizing response to DMPP persists in the presence of a blocking solution containing TTX (1 μM), CNQX (10 μM), DL-APV (50 μM), picrotoxin (50 μM), and atropine (4 μM), demonstrating that the effect is independent of synaptic transmission and is specific to nicotinic modulation. Box plot showing the depolarization response and washout phase, with significant changes observed (***$p < 0.001$, Friedman test with Wilcoxon test (Bonferroni correction)).

Video 1

A video demonstrating ChC activity was generated using GCaMP6s signals recorded over nearly four minutes (acquisition rate: 15.56 fps, accelerated to 120 fps). The video synchronizes ChC calcium signals with ball movement and pupil diameter recordings. Strikingly, the most pronounced calcium signals coincide with periods of arousal, marked by active running and significant pupil dilation.

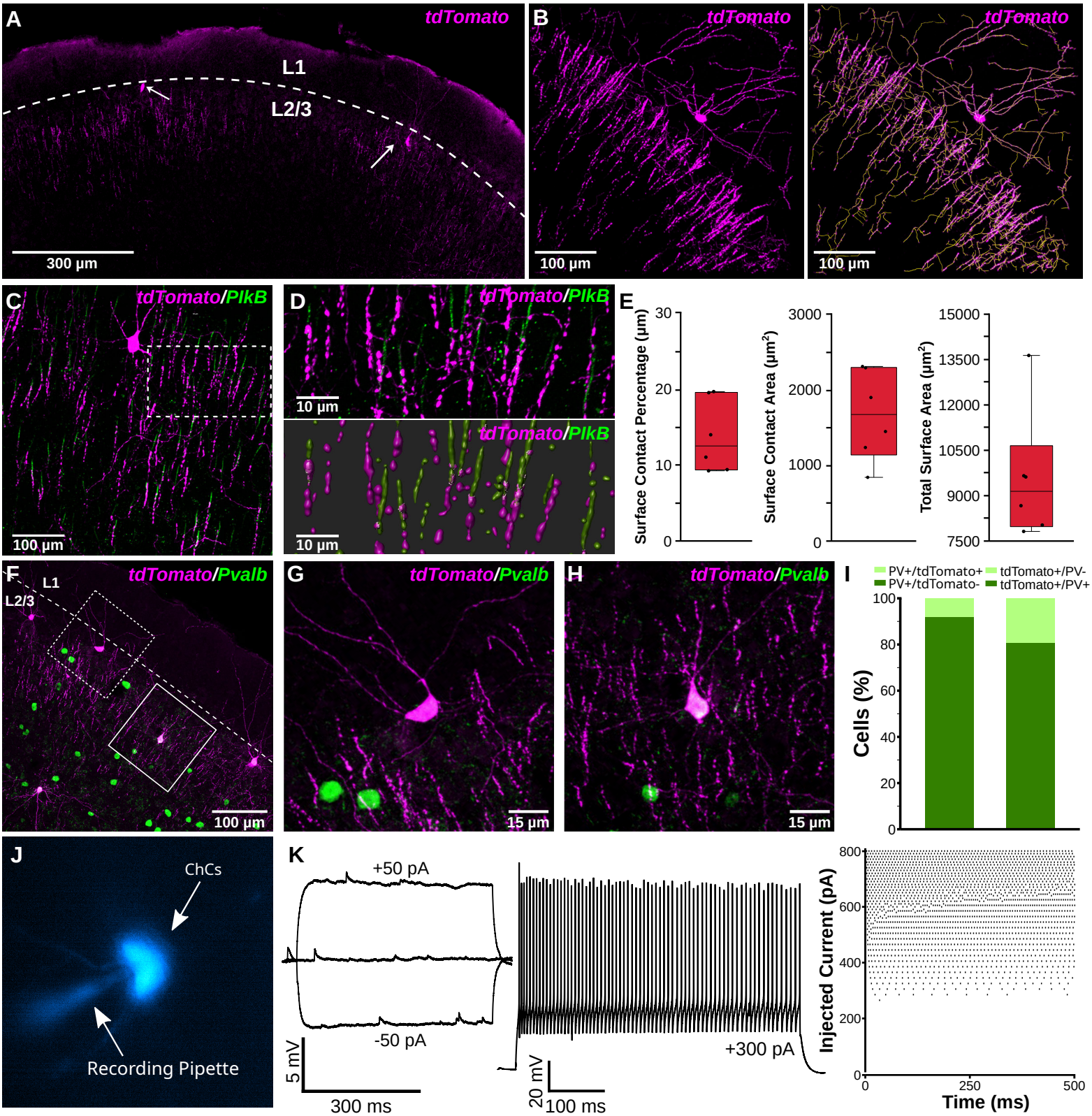
A
tdTomato
L1
L2/3
300 µm
B
tdTomato
100 µm
tdTomato
100 µm
C
tdTomato/PlkB
100 µm
D
tdTomato/PlkB
10 µm
tdTomato/PlkB
10 µm
E
Surface Contact Percentage (µm)
Surface Contact Area (µm²)
Total Surface Area (µm²)
F
tdTomato/Pvalb
L1
L2/3
100 µm
G
tdTomato/Pvalb
15 µm
H
tdTomato/Pvalb
15 µm
I
PV+/tdTomato+
PV+/tdTomato-
tdTomato+/PV-
tdTomato+/PV+
Cells (%)
J
ChCs
Recording Pipette
K
+50 pA
-50 pA
5 mV
300 ms
+300 pA
20 mV
100 ms
Injected Current (pA)
Time (ms)

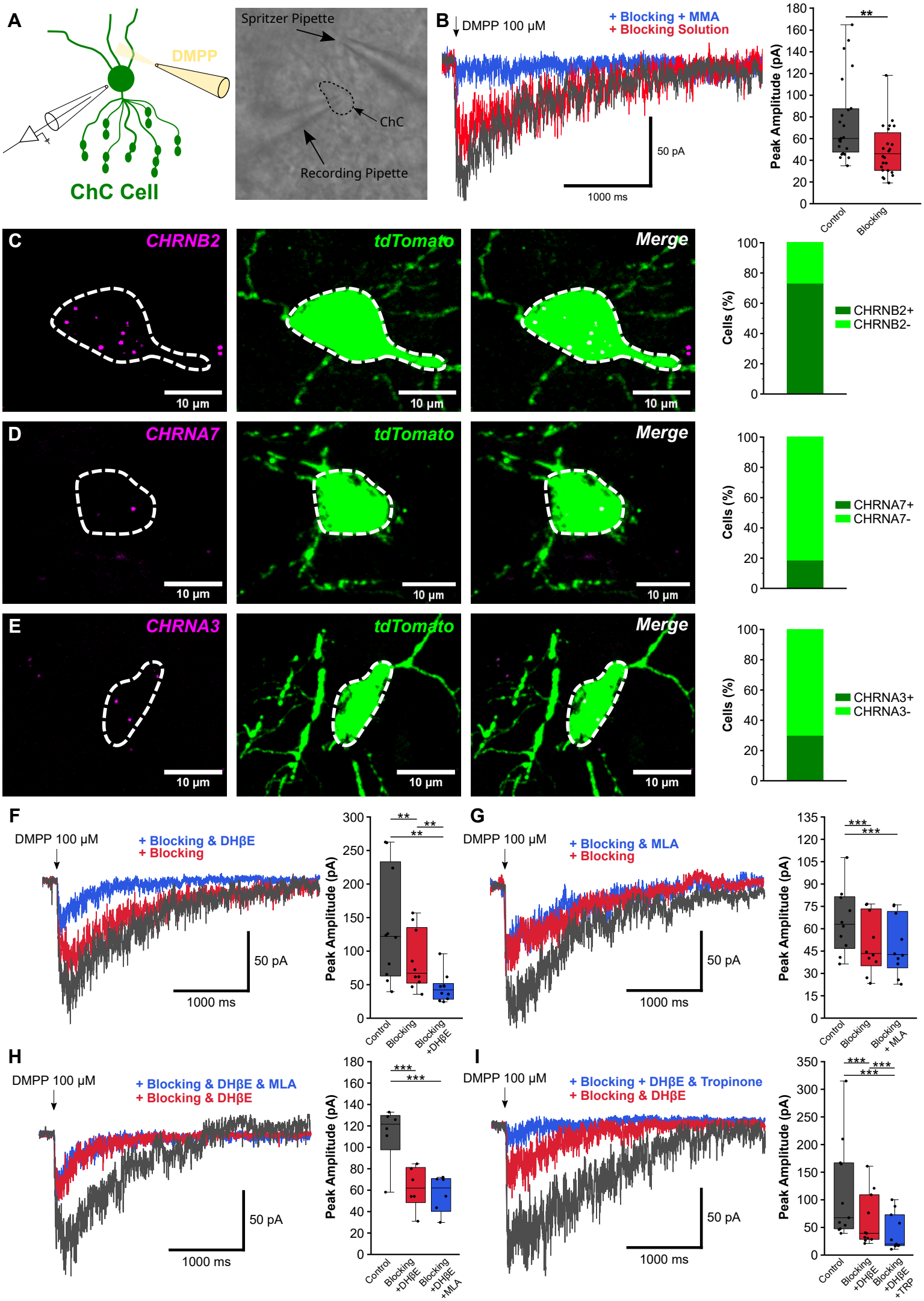
A
DMPP
ChC Cell
Spritzer Pipette
ChC
Recording Pipette
B
DMPP 100 µM
+ Blocking + MMA
+ Blocking Solution
50 pA
1000 ms
Peak Amplitude (pA)
Control
Blocking
C
CHRNB2
tdTomato
Merge
10 µm
Cells (%)
CHRNB2+
CHRNB2-
D
CHRNA7
CHRNA7+
CHRNA7-
E
CHRNA3
CHRNA3+
CHRNA3-
F
+ Blocking & DHβE
+ Blocking
Blocking +DHβE
G
+ Blocking & MLA
Blocking + MLA
H
+ Blocking & DHβE & MLA
+ Blocking & DHβE
Blocking +DHβE +MLA
I
+ Blocking + DHβE & Tropinone
+ Blocking & DHβE
Blocking +DHβE +TRP

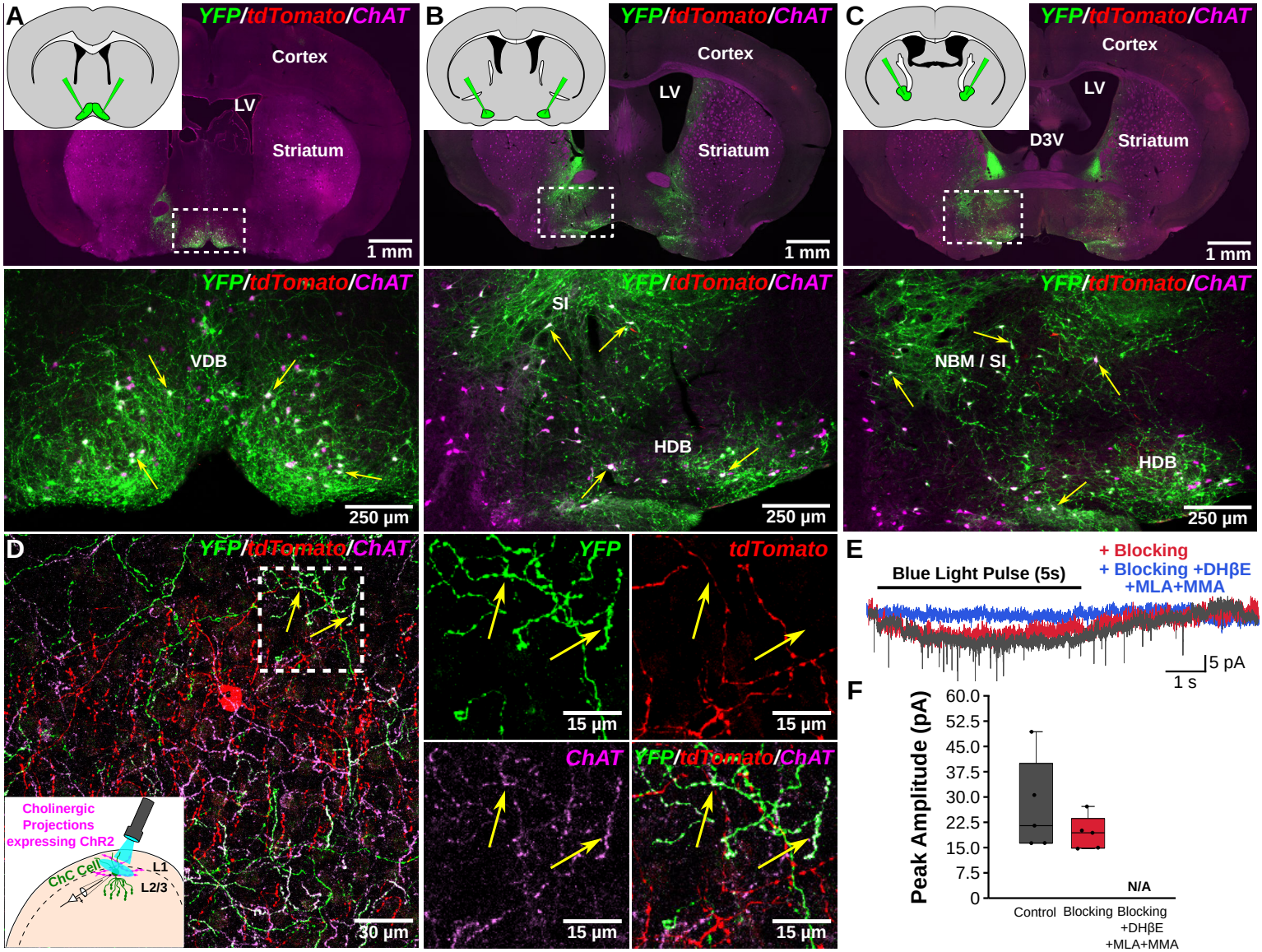
A
YFP/tdTomato/ChAT
Cortex
LV
Striatum
1 mm
B
YFP/tdTomato/ChAT
Cortex
LV
Striatum
1 mm
C
YFP/tdTomato/ChAT
Cortex
LV
D3V
Striatum
1 mm
YFP/tdTomato/ChAT
VDB
250 µm
YFP/tdTomato/ChAT
SI
HDB
250 µm
YFP/tdTomato/ChAT
NBM / SI
HDB
250 µm
D
YFP/tdTomato/ChAT
Cholinergic Projections expressing ChR2
ChC Cell
L1
L2/3
30 µm
YFP
15 µm
tdTomato
15 µm
ChAT
15 µm
YFP/tdTomato/ChAT
15 µm
E
Blue Light Pulse (5s)
+ Blocking
+ Blocking +DHβE +MLA+MMA
5 pA
1 s
F
Peak Amplitude (pA)
60.0
52.5
45.0
37.5
30.0
22.5
15.0
7.5
0
N/A
Control
Blocking
Blocking +DHβE +MLA+MMA

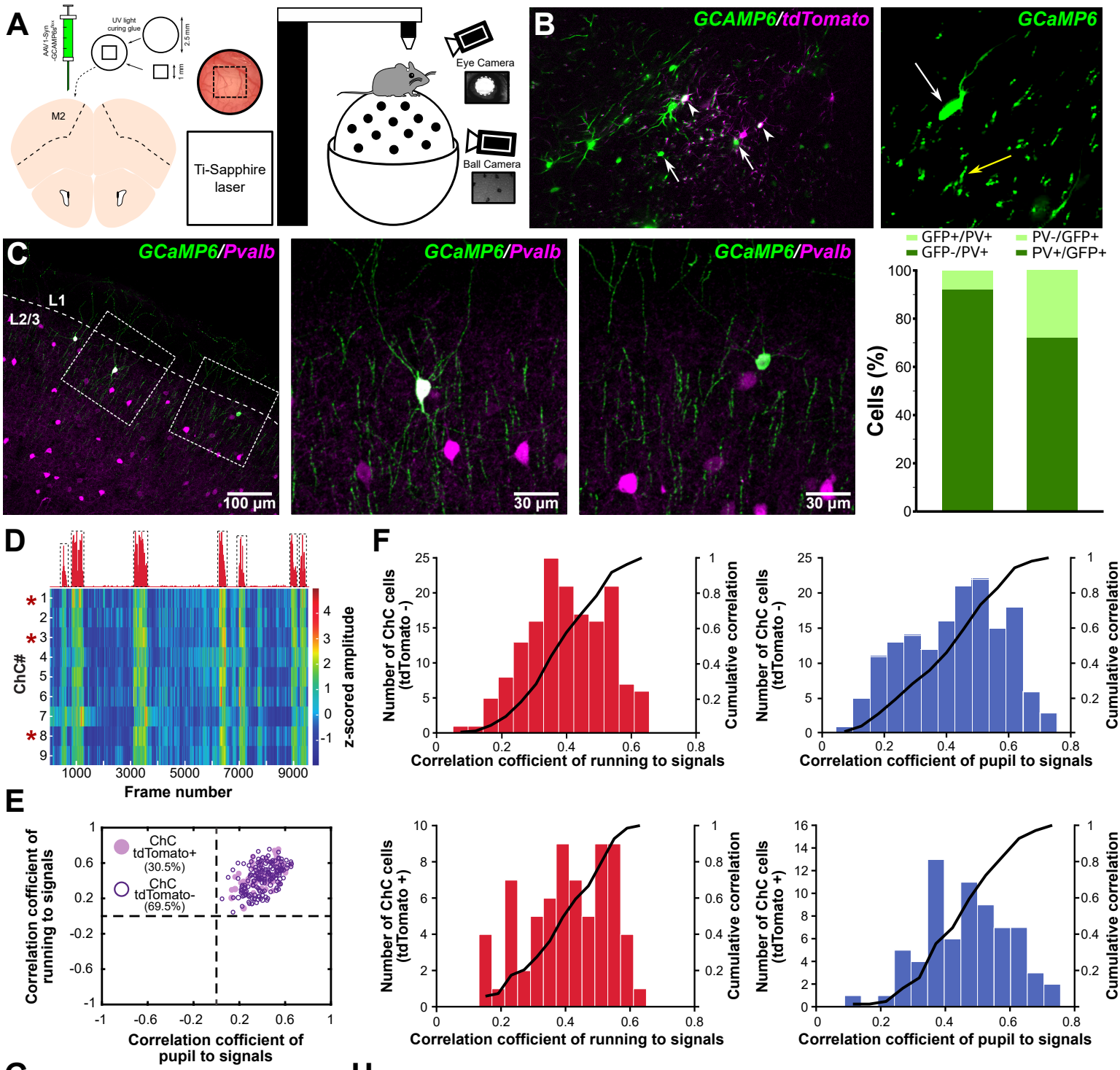
A
AAV.1-Syn -GCAMP6s
UV light curing glue
2.5 mm
1 mm
M2
Ti-Sapphire laser
Eye Camera
Ball Camera
B
GCAMP6/tdTomato
GCaMP6
C
GCaMP6/Pvalb
L1
L2/3
100 µm
30 µm
30 µm
GFP+/PV+
GFP-/PV+
PV-/GFP+
PV+/GFP+
Cells (%)
D
ChC#
z-scored amplitude
Frame number
E
ChC tdTomato+ (30.5%)
ChC tdTomato- (69.5%)
Correlation cofficient of running to signals
Correlation cofficient of pupil to signals
Number of ChC cells (tdTomato -)
Number of ChC cells (tdTomato +)
Cumulative correlation
Correlation cofficient of running to signals
Correlation cofficient of pupil to signals
F
G
Correlation index
Corr Run/Sig
Corr Pupil/Sig
H
ChC sig
Running
4 SD
60 s
ChC sig
Pupil
1 SD
6 s

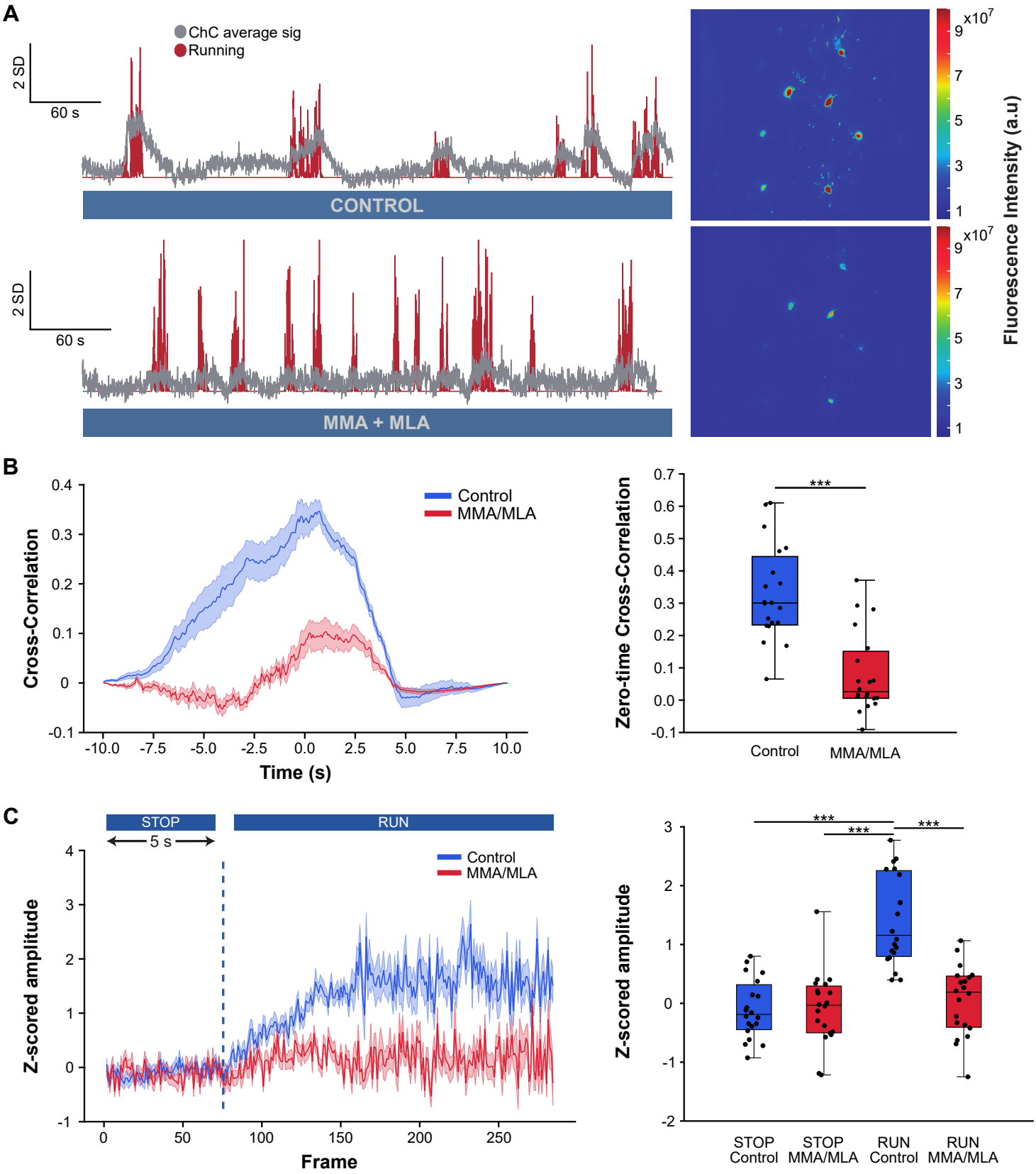
A
ChC average sig
Running
2 SD
60 s
CONTROL
MMA + MLA
x10^7
Fluorescence Intensity (a.u)
B
Control
MMA/MLA
Cross-Correlation
Time (s)
Zero-time Cross-Correlation
***
C
STOP
RUN
5 s
Z-scored amplitude
Frame
STOP Control
STOP MMA/MLA
RUN Control
RUN MMA/MLA

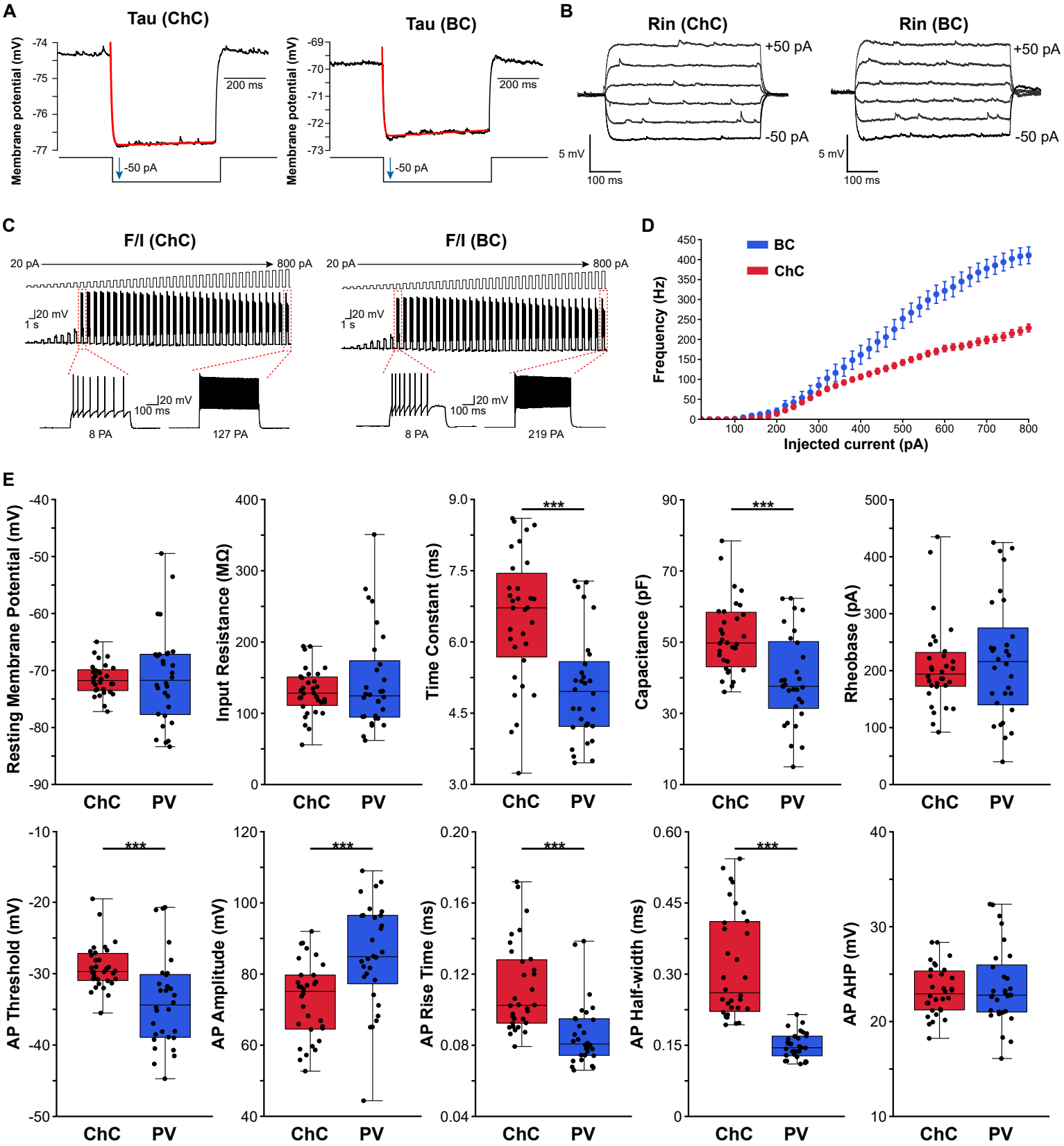
A
Tau (ChC)
Tau (BC)
Membrane potential (mV)
200 ms
-50 pA
B
Rin (ChC)
Rin (BC)
+50 pA
-50 pA
5 mV
100 ms
C
F/I (ChC)
F/I (BC)
20 pA
800 pA
20 mV
1 s
100 ms
8 PA
127 PA
219 PA
D
BC
ChC
Frequency (Hz)
Injected current (pA)
E
Resting Membrane Potential (mV)
Input Resistance (MΩ)
Time Constant (ms)
Capacitance (pF)
Rheobase (pA)
AP Threshold (mV)
AP Amplitude (mV)
AP Rise Time (ms)
AP Half-width (ms)
AP AHP (mV)
***
ChC
PV

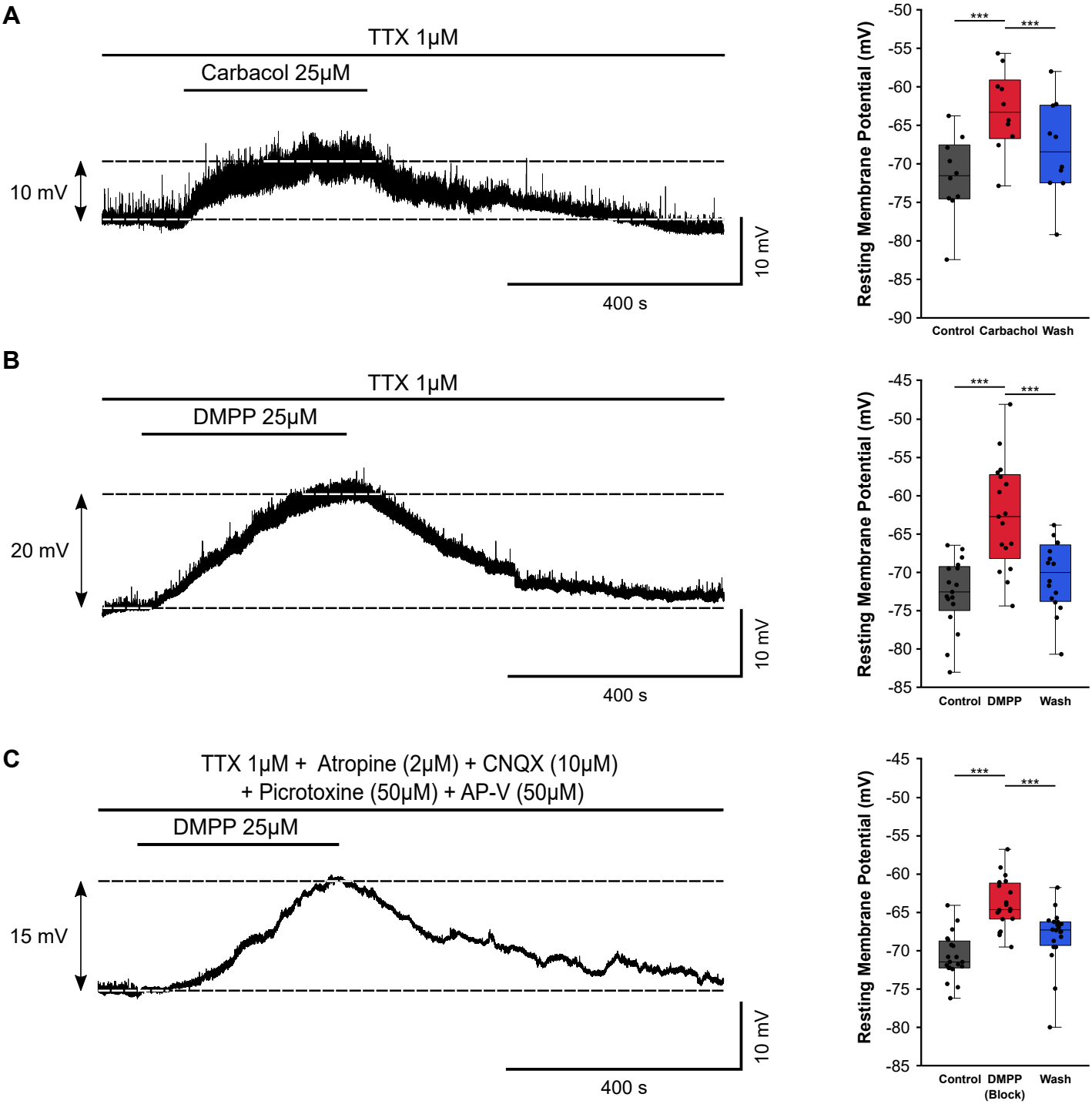
A
TTX 1μM
Carbacol 25μM
10 mV
10 mV
400 s
Resting Membrane Potential (mV)
-50
-55
-60
-65
-70
-75
-80
-85
-90
***
***
Control
Carbachol
Wash
B
TTX 1μM
DMPP 25μM
20 mV
10 mV
400 s
Resting Membrane Potential (mV)
-45
-50
-55
-60
-65
-70
-75
-80
-85
***
***
Control
DMPP
Wash
C
TTX 1μM + Atropine (2μM) + CNQX (10μM)
+ Picrotoxine (50μM) + AP-V (50μM)
DMPP 25μM
15 mV
10 mV
400 s
Resting Membrane Potential (mV)
-45
-50
-55
-60
-65
-70
-75
-80
-85
***
***
Control
DMPP
(Block)
Wash